A novel bidirectional pendulum tuned mass damper using variable homogeneous friction to achieve amplitudeindependent control

A novel bidirectional pendulum tuned mass damper using variable homogeneous friction to achieve amplitude-independent control

Emiliano Matta

Politecnico di Torino, Corso Duca degli Abruzzi 24, 10129 Turin, Italy
E-mail: emiliano.matta@polito.it · Phone: +39 011 090 4867 · ORCID: 0000-0001-5453-1470

Abstract
Passive tuned mass dampers (TMDs) are widely used in controlling structural vibrations. Although their principle is well established, the search for improved arrangements is still under way. This effort has recently produced an innovative paradigm of bidirectional pendulum TMD (BTMD) that, moving along a specially designed three-dimensional (3D) surface, can simultaneously control two in-plane orthogonal structural modes. In existing versions of BTMDs, energy dissipation is provided either by ordinary horizontal viscous dampers or by an original arrangement of vertical friction dampers. In this paper, a new paradigm is proposed, in which energy dissipation comes from the tangential friction arising along the pendulum surface out of an optimal spatially-variable friction coefficient pattern. Within this paradigm, if the friction coefficient is taken proportional to the modulus of the pendulum surface gradient, the dissipation model results nonlinear homogeneous in the small-displacement domain, and the performance of the absorber, herein called the homogeneous tangential friction BTMD (HT-BTMD), results independent from the excitation level. The present work introduces this concept, derives the analytical model of the HT-BTMD, establishes a method for its optimal design and numerically verifies its seismic effectiveness in comparison with viscously-damped devices. The validity and feasibility of the concept are demonstrated through experimental tests on a small-scale lab prototype, which also show the efficacy of a stepwise approximation of the homogeneous friction pattern. The new device proves a competing alternative to existing BTMDs, and homogeneous tangential friction proves a promising new paradigm to provide pendular systems with amplitude-independent structural damping.

Keywords: earthquake mitigation; tuned mass dampers; pendulum mechanics; nonlinear systems; bidirectional tuning; homogeneous friction damping.

1 Introduction

Tuned mass dampers (TMDs) are well-known passive vibration control systems, widely used to improve the serviceability and safety of civil structures against natural and manmade hazards [1]. In its simplest configuration, a TMD is a single-degree-of-freedom (SDOF) linear appendage of the main structure, capable to absorb mechanical energy from a target structural mode, once its frequency is tuned to the target structural frequency and its damping is optimally chosen [2]. If horizontal vibrations are of concern, one commonly adopted scheme is the pendulum TMD, which uses gravity to generate the required restoring force, and consists of a damped mass constrained to move along an arched trajectory, whose curvature determines the absorber natural frequency. Pendulum TMDs can be designed either as "supported", i.e. moving along physical tracks, or as "hanging", i.e. suspended through ropes or bars. Supported pendulums are usually more compact, durable and versatile in shape, while hanging pendulums may be easier to re-tune. Classical schemes of supported pendulum TMDs are reported in Figures 1a to 1g, including the ball pendulum [3], the rolling and sliding pendulums (with single or double cavity) [4, 5] and the rocking pendulum (in rolling or sliding versions). Classical schemes of hanging pendulum TMDs are shown in Figures 1h to 1j, including the simple pendulum, the compound pendulum and the rigid bar pendulum.

Despite the numerous schemes of pendulum TMDs already available, the search for improved configurations is still under way. In [6] an innovative unbalanced rolling pendulum TMD is presented, where the gravitational restoring force is produced not by the curvature of the supporting track (in fact flat) but by the unbalanced distribution of mass within the rolling body (Figure 1k). In [7] a novel tuned rolling-ball damper is proposed for controlling wind turbines, made of multiple steel balls rolling in a spherical recess and dissipating energy through rolling friction and impact (Figure 1l). In the context of nonlinear energy sinks (NSEs), similar to TMDs but characterized by an essentially nonlinear restoring force that allows for a broader resonance bandwidth, a new track NES is proposed in [8], based on a specially shaped, smooth and symmetrical track designed to produce the desired nonlinearizable restoring force. In [9] a new asymmetrical variant of the same track NSE is proposed, in which the smooth track nonlinearity is combined with a discontinuous impact nonlinearity.

Out of this search for new arrangements, a novel paradigm of bidirectional pendulum TMD (BTMD) has recently emerged, capable to simultaneously control two in-plane orthogonal structural modes even when their frequencies are different, by means of an optimal non-axial-symmetrical three-dimensional (3D) concave surface. Particular to this surface, and condition for the bidirectional tuning, is that its two principal meridian sections are oriented as the two target structural modes and tuned to the corresponding frequencies according to the simple pendulum law. This BTMD

paradigm has been implemented in two variants, respectively belonging to the supported and to the hanging pendulum types. The first variant is the rolling-pendulum BTMD proposed in [10] (Figure 2a). In this case, the 3D pendulum surface is ensured by special 3D rolling-pendulum bearings, made of two identical cavities symmetrical facing each other and sandwiching a rolling ball. By varying the shape of the two cavities and the radius of the rolling ball, any 3D surface can be obtained. The second variant is the hanging-pendulum BTMD proposed in [11] (Figure 2b). In this case, the 3D pendulum surface is ensured by a special Y-shaped arrangement of the suspending cables. By varying the length of the cables, any toroidal surface can be obtained.

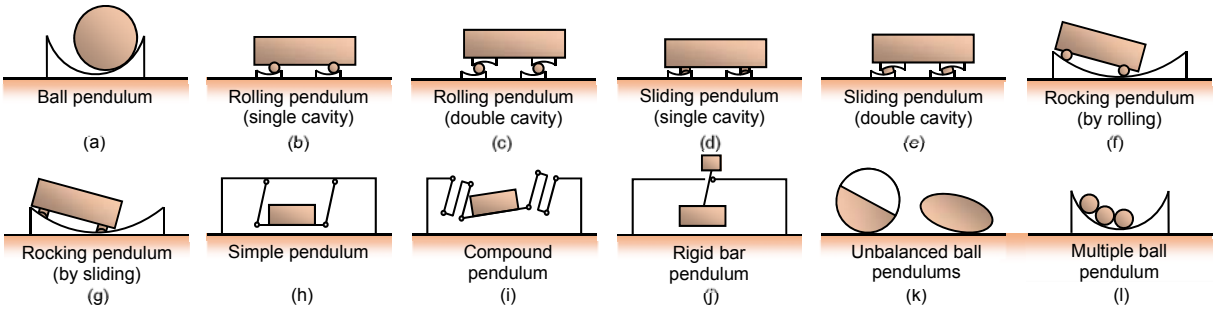

Figure 1. Possible schemes of pendulum TMDs for controlling horizontal vibrations: (a÷g) classical supported pendulums; (h÷i) classical hanging pendulums; (k) unbalanced ball pendulums [6]; (l) multiple ball pendulum [7].

In the said existing variants of BTMDs, energy dissipation is provided either by ordinary horizontal viscous dampers, proposed for the supported type in [10] (Figure 2a), or by an original vertical arrangement of a friction damper, proposed for the hanging type in [11] (Figure 2b). In this latter case, because the friction damper and the 3D surface are mutually orthogonal in the small-displacement domain, the first-order approximation of the dissipative model gets nonlinear but homogeneous [12]. As a result, the absorber exhibits an equivalent damping ratio and an effectiveness which remain constant with the amplitude of motion, contrary to what happens if the friction damper acts in the direction of motion of the absorber, in which case the equivalent damping ratio becomes inversely proportional to the amplitude and the effectiveness becomes amplitude-dependent [13].

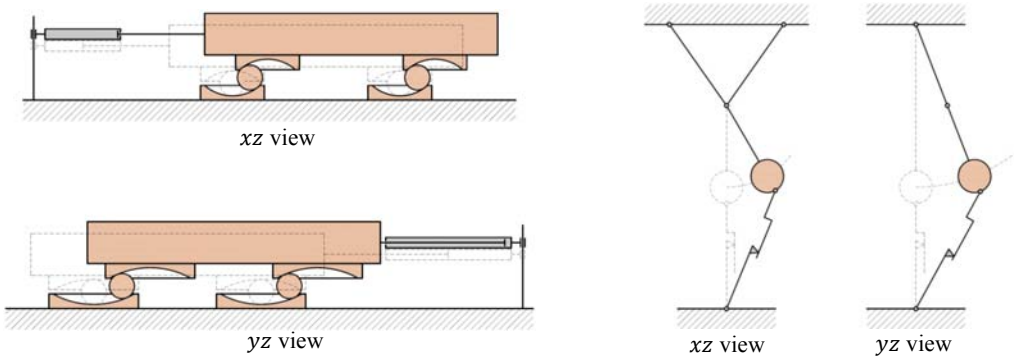

Figure 2. Existing variants of BTMD: (a) the rolling-pendulum BTMD [10]; (b) the hanging-pendulum BTMD [11].

In this paper, a new type of supported BTMD is proposed, in which energy dissipation comes from the tangential friction force which develops along the 3D guiding surface, this force being determined by a friction coefficient that varies along the surface according to an optimal geometrical pattern. In particular, if the friction coefficient varies proportionally to the modulus of the surface gradient, the dissipation model turns out to be homogeneous in the small-displacement domain and the new device, henceforth called the homogeneous tangential BTMD (HT-BTMD), achieves a control performance which is independent from the excitation level. In the novel HT-BTMD, friction can be produced either by rolling or by sliding, depending on the type of supported pendulum chosen (Figure 1). Any of the supported pendulum configurations shown in Figure 1 (i.e. a÷g and l) are eligible candidates for implementing this concept. The friction coefficient can be varied along the surface through changing the surface roughness or the type or thickness of the surface coating, either continuously (exactly according to the optimum pattern) or discretely (according to its stepwise linear approximation). With respect to the variable friction pendulum TMD proposed in [14], the HT-

BTMD shows only slight similarities, because in that case the pendulum was spherical (not a BTMD then) and, above all, the friction coefficient varied linearly but non-proportionally with the radial distance, making energy dissipation non-homogeneous. With respect to other ordinary pendulum TMDs relying on tangential friction as the damping source [e.g. 3, 15], differences are even bigger, because in those cases the friction coefficient was constant along the surface and the absorber effectiveness strongly depended on the vibration intensity. Finally, with respect to existing BTMDs configurations, which require the accommodation of appropriate viscous or friction dampers, the new HT-BTMD achieves a greater compactness, its dissipation mechanism being integral with the guiding surface. This may be particularly beneficial in some cases, for example in many applications of ball pendulum TMDs (Figure 1a) [16].
The remaining of the paper is organized as follows: in Section 2 the fully nonlinear 3D model of a BTMD with either viscous damping or variable tangential friction is derived, including its first-order approximation and its 2D reduction; in Section 3 an optimal design method is presented for both viscous and friction alternatives; in Section 4 the two alternatives are compared based on the first-order approximated model (small-displacement domain); in Section 5 the two alternatives are compared based on the fully-nonlinear model (large-displacement domain); in Section 6 a case study is shown; in Section 7 the experimental validation of the concept is offered; in Section 8 conclusions are drawn.

2. Description and modelling of the new device and of its viscous counterpart

In this section, the fully nonlinear 3D model is derived for a BTMD that incorporates: (i) one or more viscous dampers connecting it to the structure, and (ii) a variable tangential friction acting on the pendulum surface. This comprehensive model will be used in the following sections to separately simulate either the new HT-BTMD or its viscous counterpart, herein called the V-BTMD. The model is first derived for the BTMD alone and then enlarged to include the primary structure. The first-order approximation of the fully nonlinear 3D model and its subsequent reduction to a 2D model are finally presented, which will be used in Section 3 to establish an optimal design method.

2.1 Statement of the problem

A BTMD including both viscous damping and tangential friction is schematized in Figure 3. It consists of a point mass m subject to gravity g and constrained to move along a generic 3D differentiable concave-up surface, rigidly connected to the structural support in O, where the surface is minimum. The BTMD rotational inertia is neglected for simplicity. The motion of m along the surface is contrasted by three possible mechanisms, namely: (i) the viscous damper connecting m to the support in A; (ii) the tangential friction acting along the surface; and (iii) the fail-safe bumper connecting m to the support in B. Because the rotations of the structural support are here assumed negligible, the surface as well as points A and B purely translate together with the support in O.

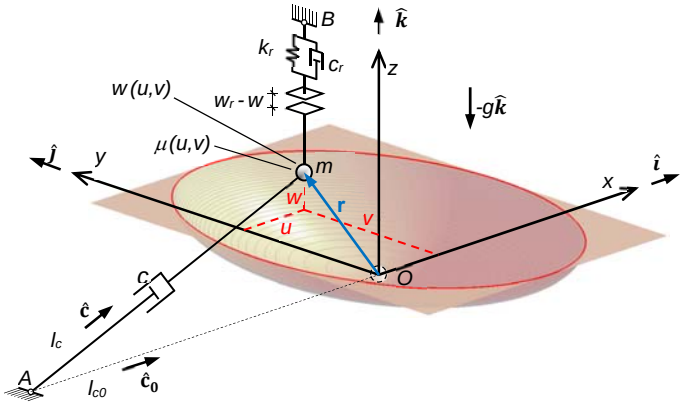

Figure 3. Axonometric scheme of the BTMD model.

Denoting by u, v and w the coordinates of m with respect to the local reference system xyz fixed to the support in O (z being the vertical axis), the pendulum kinematic constraint is given by the surface equation $w = w(u,v) = w(\boldsymbol{q})$ and the relative displacement of m is expressed by $\boldsymbol{r} = [u,v,w]^T = [\boldsymbol{q}^T, w(\boldsymbol{q})]^T$, where u and v are the two independent coordinates (Lagrangians), w is the dependent coordinate and $\boldsymbol{q} = [u,v]^T$ is the pendulum degree-of-freedom vector. Without loss of generality, x and y are set parallel to the two structural target modeshapes, here assumed mutually orthogonal in plan. Versors $\hat{\boldsymbol{\imath}}$, $\hat{\boldsymbol{\jmath}}$ and $\hat{\boldsymbol{k}}$ are associated with the x, y and z axes, respectively. The absolute acceleration vector of the structural support is defined as $\boldsymbol{a} = [a_x, a_y, a_z]^T = [\boldsymbol{a}_h{}^T, a_z]^T$, and the relative

velocity of m is derived as $\dot{\boldsymbol{r}} = \frac{\partial \boldsymbol{r}}{\partial \boldsymbol{q}}\dot{\boldsymbol{q}} = \boldsymbol{J}\dot{\boldsymbol{q}}$, where $\boldsymbol{J} = \frac{\partial \boldsymbol{r}}{\partial \boldsymbol{q}} = [\boldsymbol{I}, \nabla w \boldsymbol{J}]^T$ is the Jacobian matrix of the kinematic transformation and $\nabla w = \frac{\partial w}{\partial \boldsymbol{q}}$ is the surface gradient.

2.2 The three dissipative mechanisms

The model accounts for three distinct dissipative mechanisms. The first two mechanisms, i.e. viscous damping and tangential friction, although assumed mutually exclusive in subsequent sections for comparison, are here modelled together. The third mechanism, i.e. the fail-safe bumper, introduced to prevent excessive strokes of the absorber, is always present but operates only in the large-displacement domain. For brevity, only one arbitrarily oriented viscous damper is supposed in deriving the BTMD analytical model (Figure 3). In general, however, multiple viscous dampers may be replicated into the model, and at least two must be included if both target modes are to be controlled.

2.2.1 The viscous damper

As shown in Figure 3, the viscous damper has damping coefficient c, undeformed length l_{c0} and deformed length l_c. Denoting by $\hat{\boldsymbol{c}}_0$ and $\hat{\boldsymbol{c}}$ the versors coaxial with the damper (oriented from A to m), respectively in its undeformed and deformed position, the damper undeformed and deformed position vectors can be introduced as $\boldsymbol{l}_{c0} = l_{c0}\hat{\boldsymbol{c}}_0$ and $\boldsymbol{l}_c = l_c\hat{\boldsymbol{c}} = \boldsymbol{l}_{c0} + \boldsymbol{r}$, and the damper axial elongation computed as $s_c = l_c - l_{c0}$. The damper axial elongation rate is given as $\dot{s_c} = \left(\frac{\partial s_c}{\partial \boldsymbol{q}}\right)^T \dot{\boldsymbol{q}}$ or equivalently as $\dot{s_c} = \hat{\boldsymbol{c}}^T\dot{\boldsymbol{r}} = \hat{\boldsymbol{c}}^T\boldsymbol{J}\dot{\boldsymbol{q}}$ (by projecting the relative velocity $\dot{\boldsymbol{r}}$ on the damper versor $\hat{\boldsymbol{c}}$). Denoting as $f_c = c\dot{s_c}$ the axial force in the damper, the viscous force vector acting on m is finally $\boldsymbol{f}_c = -f_c\hat{\boldsymbol{c}}$.

2.2.2 The tangential friction

The 3D pendulum surface is characterized by a friction coefficient which spatially varies according to an assigned pattern $\mu = \mu(u, v) = \mu(\boldsymbol{q})$. For simplicity, a rigid-plastic (dry) friction model is assumed. Also, the friction coefficient is supposed independent from both the modulus and the direction of the rolling velocity, implying: (i) the identity of the static and the kinetic friction coefficients; and (ii) the isotropy of the friction coefficient. Under these assumptions, the friction force along the surface can be expressed as:

$$f_\mu = \mu(\boldsymbol{q})N \tag{1}$$

and the friction force vector acting on m as $\boldsymbol{f}_\mu = -f_\mu\hat{\boldsymbol{t}}$, where N is the modulus of the normal reaction force vector $\boldsymbol{N}$ at the contact point and $\hat{\boldsymbol{t}}$ is the tangent versor, defined by $\hat{\boldsymbol{t}} = \boldsymbol{0}$ if $\dot{\boldsymbol{r}} = \boldsymbol{0}$ and by $\hat{\boldsymbol{t}} = \dot{\boldsymbol{r}}/\|\dot{\boldsymbol{r}}\| = \boldsymbol{J}\dot{\boldsymbol{q}}/\sqrt{\dot{\boldsymbol{q}}^T\boldsymbol{J}^T\boldsymbol{J}\dot{\boldsymbol{q}}}$ if $\dot{\boldsymbol{r}} \neq \boldsymbol{0}$. Although the comprehensive model herein proposed can accommodate any possible friction pattern, this paper is mainly focused on the following law:

$$\mu(\boldsymbol{q}) = \|\boldsymbol{\mu_0}\nabla w\| \tag{2}$$

which describes a friction coefficient varying along the surface as the modulus of the surface gradient vector ∇w pre-multiplied by the diagonal friction matrix:

$$\boldsymbol{\mu_0} = \begin{bmatrix} \mu_{0x} & 0 \\ 0 & \mu_{0y} \end{bmatrix} \tag{3}$$

in which μ_{0x} and μ_{0y} are properly selected proportionality factors, here called the friction ratios along x and y. If $\mu_{0x} = \mu_{0y} = \mu_0$, the friction matrix becomes $\boldsymbol{\mu_0} = \mu_0\boldsymbol{I}$ and Eq. (2) simplifies to:

$$\mu(\boldsymbol{q}) = \mu_0\|\nabla w\| \tag{4}$$

which indeed describes a friction coefficient proportional to the surface gradient vector.

Both Eqs. (2) and (4) ensure a homogeneous first-order friction model, as will be shown later.

To clarify the geometric meaning of these patterns, assuming for example $\mu_{0x} = 0.2$ (which corresponds to optimality for a 1% mass ratio, see Table 1 next), Figure 4 shows in blue line the principal meridian section $y = 0$ of an ellipsoidal HT-BTMD having semi-axes b_x (along x) and b_z (along z), and in red line the corresponding friction pattern as defined by Eqs. (2) and (3). In particular, if the maximum vertical displacement w is limited to $w_r = b_z/2$ (blue circle) by a fail-safe bumper, the friction coefficient μ appears to vary along the section between 0 and 0.35 (red circle).

2.2.3 The fail-safe bumper

As shown in Figure 3, the bumper has stiffness k_r, damping coefficient c_r and initial clearance w_r. The bumper reacts along z whenever w gets beyond w_r, applying to m the force vector $\boldsymbol{f}_r = -f_r\hat{\boldsymbol{k}}$, where $f_r = 0$ if $w \leq w_r$ and $f_r = k_r(w - w_r) + c_r\dot{w}$ if $w > w_r$, with $\dot{w} = \nabla w^T\dot{\boldsymbol{q}}$. Although the elastic term due to k_r prevents f_r from being entirely non-conservative, the bumping mechanism will still be called here dissipative for brevity.

2.2.4 The combined effect of the three dissipative mechanisms

The total dissipative force applied to m by the three mechanisms above is given by $\boldsymbol{f}_d = \boldsymbol{f}_c + \boldsymbol{f}_\mu + \boldsymbol{f}_r$, where $\boldsymbol{f}_c$, $\boldsymbol{f}_\mu$ and $\boldsymbol{f}_r$ are specified in the previous paragraphs. By applying Newton's 2nd Law to the mass m subjected to (i) its static weight $\boldsymbol{w} = -mg\hat{\boldsymbol{k}}$, (ii) the normal reaction force $\boldsymbol{N}$, and (iii) the total dissipative force $\mathbf{f}_d$, the dynamic equilibrium equation is derived as $\boldsymbol{w} + \boldsymbol{N} + \boldsymbol{f}_d = m(\boldsymbol{a} + \ddot{\boldsymbol{r}})$, where $\boldsymbol{a} + \ddot{\boldsymbol{r}}$ is the absolute acceleration of m. By denoting respectively as $\boldsymbol{\lambda_d} = m(\boldsymbol{a} + \ddot{\boldsymbol{r}})$ and as $\boldsymbol{\lambda_s} = -\boldsymbol{w}$ the dynamic and the static interaction forces exchanged between the BTMD and its support, and by introducing the total reaction force vector $\boldsymbol{R} = \boldsymbol{N} + \boldsymbol{f}_\mu$, the same equilibrium equation provides the equalities $\boldsymbol{N} + \boldsymbol{f}_d = \boldsymbol{R} + \boldsymbol{f}_c + \boldsymbol{f}_r = \boldsymbol{\lambda_s} + \boldsymbol{\lambda_d}$, which: (i) show how the static and the dynamic interaction forces are exchanged partly through the surface (as $\boldsymbol{R}$) and partly through the viscous and bumper devices (as $\boldsymbol{f}_c + \boldsymbol{f}_r$), or equivalently partly through the total dissipative forces $\boldsymbol{f}_d$ and partly through the normal reaction force $\boldsymbol{N}$; (ii) finally allow to compute N in Eq. (1) as the modulus of the vector $\boldsymbol{N} = \boldsymbol{\lambda_s} + \boldsymbol{\lambda_d} - \boldsymbol{f}_d$.

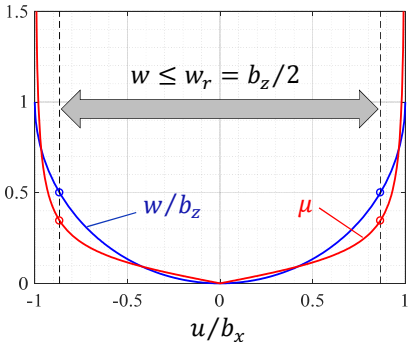

Figure 4. Principal section $y = 0$ of an ellipsoidal HT-BTMD. Blue line: pendulum profile (in terms of w/b_z). Red line: friction pattern for $\mu_{0x} = 0.2$ (in terms of μ). Blue and red circles: threshold values for $w \le w_r = b_z/2$.

2.2.5 The re-centring capability of the HT-BTMD

A fundamental property of the proposed friction pattern emerges by discussing the re-centring capability of the HT-BTMD. Assuming that the latter is at rest at $\boldsymbol{q} \neq \boldsymbol{0}$, necessary and sufficient condition for its incipient motion toward the surface centre is that the modulus of the tangential friction force, i.e. $f_\mu = \mu(\boldsymbol{q})N$, be less than the tangential component of the absorber weight, i.e. $\sqrt{(mg)^2 - N^2}$, where the normal component N of the weight is related to the surface gradient by the expression $N = mg/\sqrt{1 + \|\nabla w\|^2}$. The condition for the incipient motion is therefore $\mu(\boldsymbol{q}) < \sqrt{(mg)^2 - N^2}/N = \|\nabla w\|$, which if the friction pattern obeys Eq. (2) becomes:

$$\|\boldsymbol{\mu_0}\nabla w\| < \|\nabla w\| \tag{5}$$

This inequality is satisfied everywhere on the surface (i.e. the device has re-centring capability) if and only if $\max(\mu_{0x}, \mu_{0y}) < 1$. If $\mu_{0x} = \mu_{0y} = \mu_0$, necessary and sufficient condition for re-centring is therefore $\mu_0 < 1$, while $\mu_0 = 1$ ensures a perfect balance between gravity and friction everywhere on the surface. In conclusion, a nominal friction ratio (sufficiently) less than unity shall be adopted to ensure the re-centring of the HT-BTMD.

2.3 The fully nonlinear 3D model of the BTMD

The equation of motion of the BTMD including the three dissipation mechanisms discussed above is here derived by applying the following Euler-Lagrange equation to the mass m [11]:

$$\frac{d}{dt}\left(\frac{\partial T}{\partial \dot{\boldsymbol{q}}}\right) - \frac{\partial T}{\partial \boldsymbol{q}} + \frac{\partial V_g}{\partial \boldsymbol{q}} + \boldsymbol{Q}_i + \boldsymbol{Q}_e = \boldsymbol{0} \tag{6}$$

where $T = \frac{m}{2}\dot{\boldsymbol{r}}^T\dot{\boldsymbol{r}} = \frac{m}{2}\dot{\boldsymbol{q}}^T\boldsymbol{J}^T\boldsymbol{J}\dot{\boldsymbol{q}} = \frac{1}{2}\dot{\boldsymbol{q}}^T\boldsymbol{M}^q\dot{\boldsymbol{q}}$ is the kinetic energy of m, with $\boldsymbol{M}^q = m\boldsymbol{J}^T\boldsymbol{J}$ being its generalized mass matrix; $V_g = mgw$ is the gravitational potential energy of m; $\boldsymbol{Q}_i = -\boldsymbol{J}^T\boldsymbol{f}_d$ is the generalized internal force due to the total dissipative force $\boldsymbol{f}_d$; and $\boldsymbol{Q}_e = m\boldsymbol{J}^T\boldsymbol{a}$ is the generalized external force due to the acceleration at the structural support.

In Eq. (6), the first term is given by $\frac{d}{dt}\left(\frac{\partial T}{\partial \dot{\boldsymbol{q}}}\right) = \frac{d}{dt}(\boldsymbol{M}^q\dot{\boldsymbol{q}}) = \boldsymbol{M}^q\ddot{\boldsymbol{q}} + \dot{\boldsymbol{M}}^q\dot{\boldsymbol{q}}$, with $\dot{\boldsymbol{M}}^q = \sum_{i=1}^{2}\frac{\partial \boldsymbol{M}^q}{\partial q_i}q_i$; the second term by $\frac{\partial T}{\partial \boldsymbol{q}} = \left[\frac{\partial T}{\partial q_1} \quad \frac{\partial T}{\partial q_2}\right]^T$, with $\frac{\partial T}{\partial q_i} = \frac{\partial \dot{\boldsymbol{r}}^T}{\partial q_i}\frac{\partial T}{\partial \dot{\boldsymbol{r}}} = \left(\frac{\partial \boldsymbol{J}}{\partial q_i}\dot{\boldsymbol{q}}\right)^T m\dot{\boldsymbol{r}} = \dot{\boldsymbol{q}}^T\left(m\frac{\partial \boldsymbol{J}^T}{\partial q_i}\boldsymbol{J}\right)\dot{\boldsymbol{q}} = \dot{\boldsymbol{q}}^T\boldsymbol{H}_i\dot{\boldsymbol{q}}$; the third term by $\frac{\partial V_g}{\partial \boldsymbol{q}} = mg\nabla w$. By substituting these expressions into Eq. (6), the following nonlinear matrix differential equation is obtained, expressing the fully nonlinear 3D BTMD model:

$$\boldsymbol{M}^q\ddot{\boldsymbol{q}} + \boldsymbol{Q}_i + mg\nabla w = -m\boldsymbol{J}^T\boldsymbol{a} - \left(\dot{\boldsymbol{M}}^q\dot{\boldsymbol{q}} - \frac{\partial T}{\partial \boldsymbol{q}}\right) \tag{7}$$

In Eq. (7), the three terms on the left-hand side respectively represent the generalized inertia force vector, the generalized dissipative force vector and the generalized gravitational restoring force vector. The two terms on the right-hand side respectively represent the generalized external force vector and a second-order term that couples $\boldsymbol{q}$ and $\dot{\boldsymbol{q}}$.
The dissipative term on the left-hand side can be further developed as follow:

$$\boldsymbol{Q}_i = -\boldsymbol{J}^T\boldsymbol{f}_d = f_c\boldsymbol{J}^T\hat{\boldsymbol{c}} + f_\mu\boldsymbol{J}^T\hat{\boldsymbol{t}} + f_r\boldsymbol{J}^T\hat{\boldsymbol{k}} \tag{8}$$

where:

$$f_c\boldsymbol{J}^T\hat{\boldsymbol{c}} = \; c\dot{s}_c\boldsymbol{J}^T\hat{\boldsymbol{c}} = c[\boldsymbol{J}^T\hat{\boldsymbol{c}}\hat{\boldsymbol{c}}^T\boldsymbol{J}]\dot{\boldsymbol{q}} \tag{9}$$

$$f_\mu\boldsymbol{J}^T\hat{\boldsymbol{t}} = \; \mu(\boldsymbol{q})N\,\boldsymbol{J}^T\boldsymbol{J}\dot{\boldsymbol{q}}/\sqrt{\dot{\boldsymbol{q}}^T\boldsymbol{J}^T\boldsymbol{J}\dot{\boldsymbol{q}}} \tag{10}$$

$$f_r\boldsymbol{J}^T\hat{\boldsymbol{k}} = f_r\nabla w \tag{11}$$

represent, respectively, the generalized viscous, friction and bumper force vectors.

2.4 The fully nonlinear 3D model of the BTMD on a linear MDOF structure

If the BTMD system is mounted on a linear multi-degree-of-freedom (MDOF) structure subjected to ground acceleration, the dynamic equation of motion of the primary structure may be expressed as:

$$\boldsymbol{M}_s\ddot{\boldsymbol{q}}_s + \boldsymbol{C}_s\dot{\boldsymbol{q}}_s + \boldsymbol{K}_s\boldsymbol{q}_s + \boldsymbol{L}^T\boldsymbol{\lambda}_d = -\boldsymbol{M}_s\boldsymbol{R}_s\ddot{\boldsymbol{r}}_g \tag{12}$$

where $\mathbf{q}_s$ is the vector of structural DOFs; $\boldsymbol{M}_s$, $\boldsymbol{C}_s$ and $\boldsymbol{K}_s$ are the structural mass, damping and stiffness matrices; $\ddot{\boldsymbol{r}}_g = \left[\ddot{u}_g \;\; \ddot{v}_g \;\; \ddot{w}_g\right]^T$ is the vector of ground accelerations; $\boldsymbol{\lambda_d}$ is the dynamic interaction force vector between the BTMD and its structural support (the static interaction force vector $\boldsymbol{\lambda_s}$ having been omitted because it is irrelevant to the dynamic response); $\boldsymbol{L}$ is a kinematic transformation matrix; and $\boldsymbol{R}_s$ is the input topological matrix [11].
By expressing the absolute acceleration at the structural support as $\boldsymbol{a} = \boldsymbol{L}\left(\ddot{\boldsymbol{q}}_s + \boldsymbol{R}_s\ddot{\boldsymbol{r}}_g\right)$ and the relative acceleration of the BTMD as $\ddot{\boldsymbol{r}} = \boldsymbol{J}\ddot{\boldsymbol{q}} + \dot{\boldsymbol{J}}\dot{\boldsymbol{q}}$, the dynamic interaction force $\boldsymbol{\lambda_d}$ is given by:

$$\boldsymbol{\lambda_d} = m(\boldsymbol{a} + \ddot{\boldsymbol{r}}) = m\left(\boldsymbol{L}\ddot{\boldsymbol{q}}_s + \boldsymbol{L}\boldsymbol{R}_s\ddot{\boldsymbol{r}}_g + \boldsymbol{J}\ddot{\boldsymbol{q}} + \dot{\boldsymbol{J}}\dot{\boldsymbol{q}}\right) \tag{13}$$

By combining Eqs. (7), (12) and (13), the fully nonlinear 3D coupled equation of motion of the structure and the BTMD is finally obtained as:

$$\begin{bmatrix}\boldsymbol{M}_s + m\boldsymbol{L}^T\boldsymbol{L} & m\boldsymbol{L}^T\boldsymbol{J}\\ m\boldsymbol{J}^T\boldsymbol{L} & \boldsymbol{M}^q\end{bmatrix}\begin{bmatrix}\ddot{\boldsymbol{q}}_s\\ \ddot{\boldsymbol{q}}\end{bmatrix} + \begin{bmatrix}\boldsymbol{C}_s & \boldsymbol{0}\\ \boldsymbol{0} & \boldsymbol{0}\end{bmatrix}\begin{bmatrix}\dot{\boldsymbol{q}}_s\\ \dot{\boldsymbol{q}}\end{bmatrix} + \begin{bmatrix}\boldsymbol{0}\\ \boldsymbol{Q}_i\end{bmatrix} + \begin{bmatrix}\boldsymbol{K}_s & \boldsymbol{0}\\ \boldsymbol{0} & \boldsymbol{0}\end{bmatrix}\begin{bmatrix}\boldsymbol{q}_s\\ \boldsymbol{q}\end{bmatrix} =$$
$$= -\begin{bmatrix}\boldsymbol{M}_s + m\boldsymbol{L}^T\boldsymbol{L}\\ m\boldsymbol{J}^T\boldsymbol{L}\end{bmatrix}\boldsymbol{R}_s\ddot{\boldsymbol{r}}_g - \begin{bmatrix}m\boldsymbol{L}^T\dot{\boldsymbol{J}}\dot{\boldsymbol{q}}\\ \dot{\boldsymbol{M}}^q\dot{\boldsymbol{q}} - \frac{\partial T}{\partial \boldsymbol{q}}\end{bmatrix} \tag{14}$$

2.5 The first-order approximation of the 3D model

The first-order approximation of the fully nonlinear 3D model of the absorber is obtained by expressing each term in Eqs. (7) to (11) as a Taylor series and by truncating its higher-order terms.
In this way, the generalized inertia force vector in Eq. (7) becomes $\boldsymbol{M}^q\ddot{\boldsymbol{q}} \approx m\ddot{\boldsymbol{q}}$.
The surface gradient vector in Eq. (7) becomes $\nabla w \approx \boldsymbol{H}_w\boldsymbol{q}$, where:

$$\boldsymbol{H}_w = \begin{bmatrix}1/L_x & 0\\ 0 & 1/L_y\end{bmatrix} = \begin{bmatrix}h_{wx} & 0\\ 0 & h_{wy}\end{bmatrix} \tag{15}$$

is the Hessian matrix of $w(\boldsymbol{q})$ in $\boldsymbol{q} = \boldsymbol{0}$, and L_x and L_y are defined as the pendulum lengths along x and y.
The generalized restoring force vector in Eq. (7) becomes $mg\nabla w \approx mg\boldsymbol{H}_w\boldsymbol{q} = \boldsymbol{K}_w\boldsymbol{q}$, where:

$$\boldsymbol{K}_w = \begin{bmatrix}mg/L_x & 0\\ 0 & mg/L_y\end{bmatrix} = \begin{bmatrix}k_{wx} & 0\\ 0 & k_{wy}\end{bmatrix} \tag{16}$$

is the equivalent pendular stiffness matrix, and k_{wx} and k_{wy} represent the equivalent pendular stiffness along x and y.
The generalized viscous force vector in Eq. (9), assuming for simplicity that the viscous damper in the undeformed position is parallel to the xy plane, becomes:

$$f_c\boldsymbol{J}^T\hat{\boldsymbol{c}} \approx c[\hat{\boldsymbol{c}}_{0h}\hat{\boldsymbol{c}}_{0h}^T] = c\begin{bmatrix}\hat{c}_{0x}^2 & \hat{c}_{0x}\hat{c}_{0y}\\ \hat{c}_{0x}\hat{c}_{0y} & \hat{c}_{0y}^2\end{bmatrix}\dot{\boldsymbol{q}} = \boldsymbol{C}\dot{\boldsymbol{q}} \tag{17}$$

where $\hat{\boldsymbol{c}}_{0h} = \hat{\boldsymbol{c}}_0(1{:}2) = \left[\hat{c}_{0x}, \hat{c}_{0y}\right]^T$ and $\boldsymbol{C}$ is defined as the BTMD viscous damping matrix.
The friction coefficient in Eq. (10), assuming the friction pattern expressed by Eq. (2), becomes:

$$\mu(\boldsymbol{q}) = \|\boldsymbol{\mu_0}\nabla w\| \approx \|\boldsymbol{\mu_0}\boldsymbol{H}_w\boldsymbol{q}\| \tag{18}$$

The normal component of the reaction force vector in Eq. (10) becomes:

$$N \approx m(g + a_z) = mgN_0 \tag{19}$$

where $N_0 = N/mg = (1 + a_z/g)$ is here introduced as the weight-normalized expression of N.
The generalized friction force vector in Eq. (10), considering Eqs. (18) and (19) and observing that $\boldsymbol{J}^T\boldsymbol{J}\dot{\boldsymbol{q}} \approx \dot{\boldsymbol{q}}$ and $\sqrt{\dot{\boldsymbol{q}}^T\boldsymbol{J}^T\boldsymbol{J}\dot{\boldsymbol{q}}} \approx \sqrt{\dot{\boldsymbol{q}}^T\dot{\boldsymbol{q}}} = \|\dot{\boldsymbol{q}}\|$, becomes:

$$f_\mu \boldsymbol{J}^T\hat{\boldsymbol{t}} \approx mgN_0\|\boldsymbol{\mu_0}\boldsymbol{H}_w\boldsymbol{q}\|\,\dot{\boldsymbol{q}}/\|\dot{\boldsymbol{q}}\| = N_0\|\boldsymbol{\mu_0}\boldsymbol{K}_w\boldsymbol{q}\|\,\dot{\boldsymbol{q}}/\|\dot{\boldsymbol{q}}\| \tag{20}$$

The generalized bumper force in Eq. (11), admitting that the bumper is not activated in the small-displacement domain, becomes $f_r\boldsymbol{J}^T\hat{\boldsymbol{k}} = \boldsymbol{0}$.
The generalized external force vector becomes $-m\boldsymbol{J}^T\boldsymbol{a} = -m\boldsymbol{a}_h - m\nabla w \approx -m\boldsymbol{a}_h - a_z/g\,\boldsymbol{K}_w\boldsymbol{q}$, where $\boldsymbol{a}_h = \boldsymbol{a}(1{:}2) = \left[a_x, a_y\right]^T$ and $a_z = \boldsymbol{a}(3)$ are the horizontal and vertical components of the vector of support accelerations.
Finally, the second-order term in Eq. (7) becomes $\dot{\boldsymbol{M}}^q\dot{\boldsymbol{q}} - \frac{\partial T}{\partial \boldsymbol{q}} \approx \boldsymbol{0}$.
With the approximations explained above, the first-order 3D model of the BTMD is obtained as:

$$m\ddot{\boldsymbol{q}} + \boldsymbol{C}\dot{\boldsymbol{q}} + N_0\boldsymbol{K}_w\boldsymbol{q} + N_0\|\boldsymbol{\mu_0}\boldsymbol{K}_w\boldsymbol{q}\|\,\dot{\boldsymbol{q}}/\|\dot{\boldsymbol{q}}\| = -m\boldsymbol{a}_h \tag{21}$$

and the first-order 3D model of the coupled structure-BTMD system as:

$$\begin{bmatrix}\boldsymbol{M}_s + m\boldsymbol{L}_h^T\boldsymbol{L}_h & m\boldsymbol{L}_h^T \\ m\boldsymbol{L}_h & m\boldsymbol{I}\end{bmatrix}\begin{bmatrix}\ddot{\boldsymbol{q}}_s \\ \ddot{\boldsymbol{q}}\end{bmatrix} + \begin{bmatrix}\boldsymbol{C}_s & \boldsymbol{0} \\ \boldsymbol{0} & \boldsymbol{C} + N_0\,\|\boldsymbol{\mu_0}\boldsymbol{K}_w\boldsymbol{q}\|/\|\dot{\boldsymbol{q}}\|\end{bmatrix}\begin{bmatrix}\dot{\boldsymbol{q}}_s \\ \dot{\boldsymbol{q}}\end{bmatrix} + \\ + \begin{bmatrix}\boldsymbol{K}_s & \boldsymbol{0} \\ \boldsymbol{0} & N_0\boldsymbol{K}_w\end{bmatrix}\begin{bmatrix}\boldsymbol{q}_s \\ \boldsymbol{q}\end{bmatrix} = -\begin{bmatrix}\boldsymbol{M}_s + m\boldsymbol{L}_h^T\boldsymbol{L}_h \\ m\boldsymbol{L}_h\end{bmatrix}\boldsymbol{R}_s\ddot{\boldsymbol{r}}_g \tag{22}$$

where $\boldsymbol{L}_h = \boldsymbol{L}(1{:}2)$ are the first two columns of $\boldsymbol{L}$.
Based on Eq. (21) the following comments can be made, regarding the first-order 3D model of the absorber:
(i) the inertia force vector $m\ddot{\boldsymbol{q}}$ and the restoring force vector $N_0\boldsymbol{K}_w\boldsymbol{q}$ are linear and uncoupled along x and y; if the viscous dampers are parallel to the horizontal plane, as here assumed, the viscous force vector $\boldsymbol{C}\dot{\boldsymbol{q}}$ is linear too and independent from the length of the dampers, though not uncoupled along x and y unless the dampers are parallel to these axes, as expressed by Eq. (17);
(ii) through the N_0 coupling term, the vertical support acceleration a_z affects the horizontal response of the BTMD even in the first-order approximated model, entering both the restoring force vector and the friction force vector;
(iii) the modulus of the friction force vector is $N_0\|\boldsymbol{\mu_0}\boldsymbol{K}_w\boldsymbol{q}\|$ and its direction is that of the tangent versor $\dot{\boldsymbol{q}}/\|\dot{\boldsymbol{q}}\|$; both its modulus and its direction are coupled along x and y and are nonlinear functions of $\boldsymbol{q}$ and $\dot{\boldsymbol{q}}$; the friction force vector can also be seen as the product of $\dot{\boldsymbol{q}}$ times a highly nonlinear scalar function of $\boldsymbol{q}$ and $\dot{\boldsymbol{q}}$ expressed by $N_0\|\boldsymbol{\mu_0}\boldsymbol{K}_w\boldsymbol{q}\|/\|\dot{\boldsymbol{q}}\|$, which again couples x and y directions; in short, the friction force vector is highly nonlinear and coupled;
(iv) on the other hand, because its modulus increases proportionally with $\boldsymbol{q}$, the friction force vector is a homogeneous function of $\boldsymbol{q}$ and $\dot{\boldsymbol{q}}$; because all terms on the left-hand side of Eq. (21) are also homogeneous, the equation itself is homogeneous and its solution is proportional to the horizontal acceleration $\boldsymbol{a}_h$ appearing on the right-hand side (yet not to the vertical acceleration a_z), which makes the proposed BTMD a first-order nonlinear but homogeneous system.

2.6 The simplified 2D model

In order to establish an optimal design procedure for the absorber, it is convenient to further simplify the 3D first-order models in Eqs. (21) and (22) by additionally assuming that: (i) the motion occurs in one vertical coordinate plane only, so the 3D models degenerate into 2D models in that plane; (ii) in that plane the structural target frequency is far from all other structural frequencies, so the MDOF structure can be represented by a 1DOF mode-generalized system [2]; (iii) the vertical acceleration input a_z is negligible, so $N_0 = 1$. Under these conditions, assuming without loss of generality the said vertical plane as xz, Eqs. (21) and (22) respectively become:

$$m\ddot{u} + c_x\dot{u} + k_{wx}[1 + \text{sign}(u\dot{u})\mu_{0x}]u = -ma_x \tag{23}$$

and:

$$\begin{bmatrix}m_{sx} + m & m \\ m & m\end{bmatrix}\begin{bmatrix}\ddot{u}_s \\ \ddot{u}\end{bmatrix} + \begin{bmatrix}c_{sx} & 0 \\ 0 & c_x\end{bmatrix}\begin{bmatrix}\dot{u}_s \\ \dot{u}\end{bmatrix} + \begin{bmatrix}k_{sx} & 0 \\ 0 & k_{wx}[1 + \text{sign}(u\dot{u})\mu_{0x}]\end{bmatrix}\begin{bmatrix}u_s \\ u\end{bmatrix} = \\ = -\begin{bmatrix}m_{sx} + m \\ m\end{bmatrix}\ddot{u}_g \tag{24}$$

where u_s is the structural horizontal displacement relative to the ground; m_{sx}, c_{sx} and k_{sx} are the generalized structural mass, damping coefficient and stiffness along x; and c_x is the BTMD viscous damping coefficient along x.
Dividing Eq. (23) and the second line of Eq. (24) by m, and the first line of Eq. (24) by m_{sx}, Eqs. (23) and (24) can be conveniently recast in modal terms as follows:

$$\ddot{u} + 2\zeta_x\omega_x\dot{u} + \omega_x^2[1 + \text{sign}(u\dot{u})\mu_{0x}]u = -a_x \tag{25}$$

$$\begin{bmatrix}1 + m_{Rx} & m_{Rx} \\ 1 & 1\end{bmatrix}\begin{bmatrix}\ddot{u}_s \\ \ddot{u}\end{bmatrix} + 2\omega_{sx}\begin{bmatrix}\zeta_{sx} & 0 \\ 0 & \zeta_x\omega_{Rx}\end{bmatrix}\begin{bmatrix}\dot{u}_s \\ \dot{u}\end{bmatrix} + \omega_{sx}^2\begin{bmatrix}1 & 0 \\ 0 & \omega_{Rx}^2[1 + \text{sign}(u\dot{u})\mu_{0x}]\end{bmatrix}\begin{bmatrix}u_s \\ u\end{bmatrix} =$$

$$= -\begin{bmatrix} 1 + m_{Rx} \\ 1 \end{bmatrix} \ddot{u}_g \tag{26}$$

where $m_{Rx} = m/m_{sx}$ is the BTMD mass ratio along x; $\omega_{sx} = \sqrt{k_{sx}/m_s}$ and $\omega_x = \sqrt{g/L_x} = \sqrt{k_{wx}/m}$ are the circular frequencies along x of the structure and the BTMD; $\omega_{Rx} = \omega_x/\omega_{sx}$ is the BTMD frequency ratio along x; and $\zeta_{sx} = c_{sx}/(2\omega_{sx}m_{sx})$ and $\zeta_x = c_x/(2\omega_x m)$ are the viscous damping ratios along x of the structure and the BTMD.
According to Eq. (26), once the structure and the external input are assigned, the response of the system entirely depends on the four dimensionless parameters m_{Rx}, ω_{Rx}, ζ_x and μ_{0x}, which completely define the BTMD and whose optimization is left to the following Section 3.

3. The design method

In this section, a design method is proposed for a BTMD of either viscous type (V-BTMD) or homogeneous tangential friction type (HT-BTMD). The models derived in Section 2 are used to represent both types, by in turn annulling the friction or the viscous terms. For both types, the method consists of a two-step procedure which comprises: (i) an optimization stage, providing the BTMD parameters that optimize the first-order response of the structure-TMD system, and (ii) an integration stage, providing the remaining BTMD parameters. The resulting optimal BTMDs will be extensively simulated in later sections.

3.1 The optimization stage

Optimization is the first stage of the proposed design method. It is based on the simplified 2D structure-BTMD model described by Eq. (26), linear for the V-BTMD and nonlinear but homogeneous for the HT-BTMD. As already stressed, this is a first-order, planar model that assumes a SDOF structure and no vertical ground acceleration. These features make it suitable for optimization. The adoption of a first-order model makes the design independent from the excitation level and from all BTMD geometrical parameters except the two pendulum lengths (thus excluding, e.g., the actual shape of the pendulum away from the origin, the length of the viscous dampers and all bumper features). The adoption of a planar model avoids the complications inherent in the coupling friction term, and allows optimizing separately in the two principal directions of the structure. The assumption of a SDOF structure and a horizontal input restricts the range of possible design scenarios to the most typical ones.
Based on Eq. (26), optimization is here formulated in the classical framework of H_∞ design, consisting in the minimization of the worst-case steady-state structural response to a unit-amplitude harmonic input [17]. Assuming the structure known and the BTMD mass ratio fixed according to cost-benefit expectations, the only two available free parameters, i.e. the frequency and damping ratios for the V-BTMD and the frequency and friction ratios for the HT-BTMD, are determined by minimizing the H_∞ norm of some meaningful input-output transfer function of the combined system. Assuming that the planar motion occurs in the xz plane and denoting with ω the circular frequency of the input, the transfer function here considered for design, denoted as $T_{u_s\ddot{u}_g}(\omega)$, is the ground acceleration-to-displacement transfer function, computed from $\ddot{u}_g$ to u_s. Introducing the response ratio $R_x = \left\|T_{u_s\ddot{u}_g}\right\|_\infty^{con} \Big/ \left\|T_{u_s\ddot{u}_g}\right\|_\infty^{unc}$ as the ratio of the controlled to the uncontrolled H_∞ norm of the said transfer function, optimization is formalized as the following min.max. problem:
(i) for the V-BTMD:

$$R_{xopt} = \min_{\omega_{Rx},\zeta_x} R_x = \min_{\omega_{Rx},\zeta_x} \max_{\omega} \left|T_{u_s\ddot{u}_g}(\omega)\right|^{con} \Big/ \left\|T_{u_s\ddot{u}_g}\right\|_\infty^{unc} \tag{27}$$

which provides the V-BTMD optimal parameters ω_{Rxopt} and ζ_{xopt};
(ii) for the HT-BTMD:

$$R_{xopt} = \min_{\omega_{Rx},\mu_{0x}} R_x = \min_{\omega_{Rx},\mu_{0x}} \max_{\omega} \left|T_{u_s\ddot{u}_g}(\omega)\right|^{con} \Big/ \left\|T_{u_s\ddot{u}_g}\right\|_\infty^{unc} \tag{28}$$

which provides the HT-BTMD optimal parameters ω_{Rxopt} and μ_{0xopt}.
Because R_x only depends on the structural damping ratio ζ_{sx} and on the dimensionless BTMD parameters, the optimal solutions of Eqs. (27) and (28) entirely depend on ζ_{sx} and on m_{Rx}.
For the V-BTMD (linear model), Eq. (27) has already been solved in the literature. If the structure is undamped, a closed-form solution is available [2], otherwise a numerical optimization is required [10, 18].
For the HT-BTMD (nonlinear homogeneous model), instead, Eq. (28) is new. Indeed, the only optimization so far reported of homogeneous friction TMDs is the H_2 design approach addressed in [12] and later used in [11], meant to minimize the mean square structural response to white-noise support excitation. Compared with the viscous problem, the friction problem has the inconvenience that no analytical expression exists for the transfer function. The modulus of the transfer function at ω must be computed by simulating the structural response time-history to the corresponding harmonic input until the response amplitude stabilizes with an acceptable tolerance.

Apart from this difference, Eqs. (27) and (28) are herein solved using a branch and bound search algorithm like the one adopted in [5], followed by a nonlinear least-square solver for improved local convergence.
For $\zeta_{sx} = 2\%$ and $m_{Rx} = 3\%$, results are exemplified in Figure 5. In it, the optimal V-BTMD and the optimal HT-BTMD show similar transfer functions, yet the HT-BTMD transfer function is slightly lower and shifted rightwards.

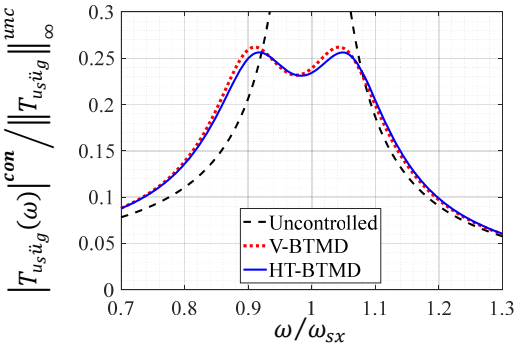

Figure 5. Normalized transfer functions from the ground acceleration to the structural displacement. Uncontrolled and optimally controlled structure with either a V-BTMD or a HT-BTMD, for ζ_{sx} = 2% and m_{Rx} = 3%.

Figure 6 reports, for the same two devices, the time response of the system under the first 20 cycles of a sinusoidal input $\ddot{u}_g = \ddot{u}_{g0}\sin(\omega_{sx}t)$ applied at the frequency of the uncontrolled structure. For greater generality, all displacements are normalized to the static displacement amplitude $u_{s0} = -\ddot{u}_{g0}/\omega_{sx}^2$ and all forces to the equivalent force amplitude $-m_{sx}\ddot{u}_{g0}$. In particular, Figures 6a and 6b respectively show the time-histories of the displacements of the structure and the BTMD, while Figure 6c shows the hysteresis loops of the BTMD, with f_{dx} denoting the component along x of the dissipative force $\boldsymbol{f}_d$, given by $f_{dx} = -f_c\hat{c}_{0x} = -c_x\dot{u}$ for the V-BTMD and by $f_{dx} = -\text{sign}(\dot{u})f_\mu = -\text{sign}(\dot{u})k_{wx}\mu_{0x}|u|$ for the HT-BTMD. Coherently with Figure 5, Figures 6a and 6b show that the time responses of the structure and the absorber are similar for the two BTMD types. Figure 6c more clearly highlights the different constitutive relationships of the two mechanisms, with the V-BTMD exhibiting the elliptic loops typical of viscous damping and the HT-BTMD showing the triangular cycles peculiar to homogeneous friction [12]. Although the steady-state amplitude of the dissipative force is higher for the HT-BTMD than for the V-BTMD (in fact by a factor close to $\pi/2$), their hysteretic loops nearly encircle the same area, globally providing a similar reduction of the structural displacement.
Figure 7 and Table 1 show the results of the optimization conducted for the two BTMD types by fixing ζ_{sx} at 2% and by varying m_{Rx} from 1‰ to 20%. It can be observed that: (i) for the V-BTMD (red curves) well know trends are obtained, decreasing from unity for ω_{Rxopt} and R_{xopt} and increasing from zero for ζ_{xopt}; the corresponding numerical values reported in Table 1 are in excellent agreement with those presented in [18]; (ii) for the HT-BTMD (blue curves) a decreasing trend starting from unity is still obtained for ω_{Rxopt}, although sensibly flatter than the corresponding trend obtained for the V-BTMD; therefore, as long as harmonic excitations are to be controlled, the ω_{Rxopt} obtained for the viscous type is far from optimal for the homogenous friction type, in contradistinction from what obtained by statistical linearization in [12] for white noise ground accelerations, where the same ω_{Rxopt} is reported for the two types; (iii) for the HT-BTMD an increasing trend starting from zero is obtained for μ_{0xopt}; if μ_{0xopt} is divided by π, the resulting curve is lower than the curve for ζ_{xopt} but convergent to it as m_{Rx} tends to zero; because μ_{0xopt}/π is the equivalent damping ratio of a homogeneous friction TMD according to [11], this convergence suggests that the viscous equivalence indeed provides the optimal μ_{0x} only for small values of m_{Rx}, i.e. when in fact the viscous and friction optimal frequency ratios ω_{Rxopt} coincide; (iv) for the HT-BTMD a decreasing trend for R_{xopt} is obtained similar to that obtained for the V-BTMD; however, R_{xopt} is always favourably smaller for the HT-BTMD, especially as m_{Rx} increases; this is an interesting new result of the present work, showing that, if properly optimized, homogeneous friction works even better than viscous damping.
What shown above along x obviously holds along y too, as long as the two corresponding 2D models are uncoupled. Assuming, as it will be done in the sequel for simplicity, that the structural target modes along x and y have the same damping ratio and the same generalized mass (i.e. $\zeta_{sx} = \zeta_{sy} = \zeta_s$ and $m_{sx} = m_{sy} = m_s$, the latter condition also implying $m_{Rx} = m_{Ry} = m_R$), the optimal dimensionless BTMD parameters along x and y turn out to coincide, i.e.

$\omega_{Rxopt} = \omega_{Ryopt} = \omega_{Ropt}$, $\zeta_{xopt} = \zeta_{yopt} = \zeta_{opt}$ and, particularly, $\mu_{0xopt} = \mu_{0yopt} = \mu_{0opt}$. The optimal friction pattern is in this case ensured by Eq. (4), by merely taking $\mu_0 = \mu_{0opt}$.

The optimal dimensionless parameters ω_{Ropt}, ζ_{opt} and μ_{0opt} can then be used, together with m_R and with the known structural parameters, to determine all BTMD dimensional parameters involved in the first-order model, including: the mass of the absorber ($m = m_R m_s$); the pendulum frequencies ($\omega_x = \omega_{Ropt}\omega_{sx}$ and $\omega_y = \omega_{Ropt}\omega_{sy}$) and lengths ($L_x = g/\omega_x^2$ and $L_y = g/\omega_y^2$); the damping coefficients for the V-BTMD ($c_x = 2\zeta_{opt}\omega_x m$ and $c_y = 2\zeta_{opt}\omega_y m$, assuming one damper along each horizontal axis); and the friction pattern around the origin for the HT-BTMD ($\mu = \mu_{0opt}\|\nabla w\| = \mu_{0opt}\sqrt{u^2/L_x^2 + v^2/L_y^2}$). The remaining BTMD parameters, involved beyond the range of small displacements, can be determined as explained in Section 3.2 next.

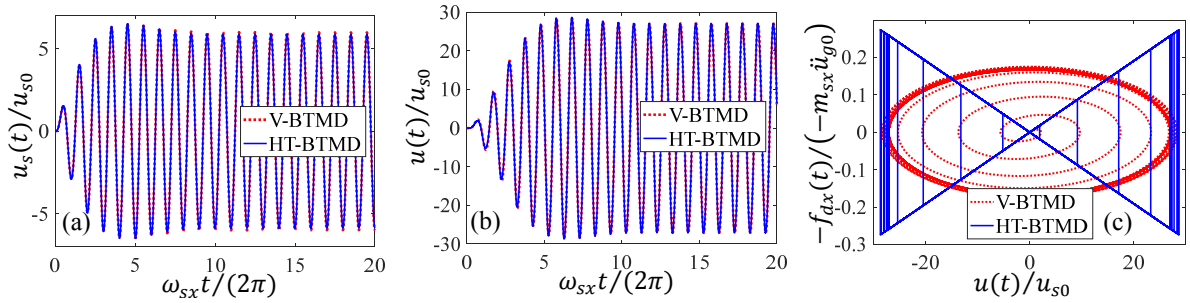

Figure 6. Time response of a structure subjected to $\ddot{u}_g = \ddot{u}_{g0}\sin(\omega_{sx}t)$ and optimally controlled by a V-BTMD or a HT-BTMD, for ζ_{sx} = 2% and m_{Rx} = 3%, in terms of: (a) structural displacement; (b) BTMD displacement; (c) BTMD constitutive law.

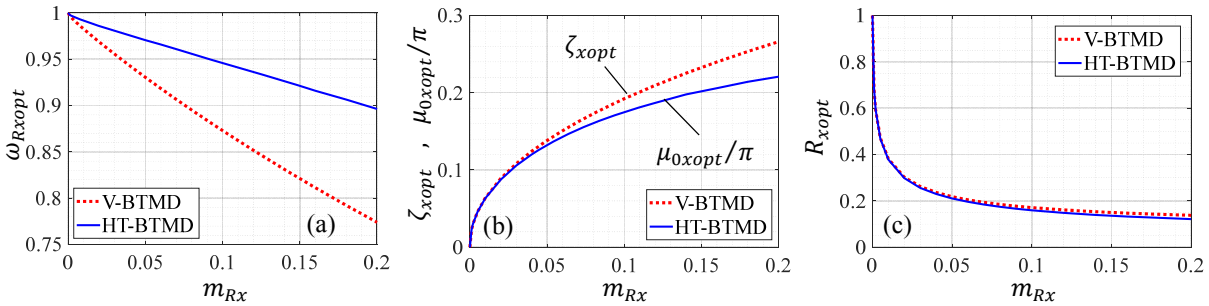

Figure 7. H∞ optimal design of a V-BTMD (red lines) and a HT-BTMD (blue lines), for ζ_{sx} = 2% and as a function of m_{Rx}, in terms of: (a) the optimal frequency ratios; (b) the optimal viscous and friction damping ratios; (c) the optimal response ratios.

Table 1. H∞ optimal design of a V-BTMD and a HT-BTMD, for ζ_{sx} = 2% and as a function of m_{Rx}.

m_{Rx}	V-BTMD			HT-BTMD		
	ω_{Rxopt}	ζ_{xopt}	R_{xopt}	ω_{Rxo_j}	μ_{0xopt}	R_{xopt}
0.001	0.9968	0.0222	0.6811	0.9979	0.0697	0.6805
0.002	0.9950	0.0302	0.5922	0.9970	0.0948	0.5914
0.005	0.9901	0.0461	0.4696	0.9948	0.1445	0.4679
0.010	0.9826	0.0639	0.3811	0.9916	0.1991	0.3784
0.020	0.9687	0.0890	0.3022	0.9859	0.2750	0.2979
0.030	0.9555	0.1082	0.2620	0.9807	0.3314	0.2563
0.040	0.9428	0.1242	0.2363	0.9756	0.3773	0.2295
0.050	0.9304	0.1382	0.2181	0.9706	0.4153	0.2103
0.060	0.9184	0.1508	0.2043	0.9658	0.4492	0.1956
0.070	0.9066	0.1623	0.1934	0.9609	0.4791	0.1839
0.080	0.8951	0.1729	0.1846	0.9558	0.5045	0.1743
0.090	0.8839	0.1829	0.1772	0.9509	0.5281	0.1663
0.100	0.8729	0.1922	0.1710	0.9459	0.5490	0.1594
0.120	0.8516	0.2095	0.1609	0.9361	0.5872	0.1482
0.140	0.8311	0.2253	0.1531	0.9265	0.6212	0.1394
0.160	0.8114	0.2398	0.1469	0.9160	0.6468	0.1323
0.180	0.7923	0.2534	0.1419	0.9064	0.6727	0.1265
0.200	0.7740	0.2661	0.1377	0.8963	0.6937	0.1216

3.2 The integration stage

The integration stage is the last stage of the design method. It is intended to provide the BTMD parameters which, intervening only in the large-displacement domain, are excluded from optimization. These parameters include the shape of the pendulum surface far from the origin, the length of the viscous dampers and the bumper characteristics. They also include the friction pattern far from the origin, unless already fixed by pre-determined laws like e.g. Eq. (4). Although these parameters too could be the object of a specific optimization based on the fully nonlinear model, in this paper they are left to the sensibility of the designer. This section discusses possible criteria for their selection.

3.2.1 The pendulum shape

The optimal pendulum lengths obtained in Section 3.1 completely identify the guiding surface around the origin. Far from it, however, infinite surfaces correspond to the desired L_x and L_y.

In what follows, the ellipsoidal shape is adopted for example. The search for better options, including for instance the torus [10, 11], is left to future studies. The surface equation is then set as

$$w(u,v) = b_z\left(1-\sqrt{1-u^2/b_x^2-v^2/b_y^2}\right) \tag{29}$$

which represents the lower half of an ellipsoid having semi-axes b_x, b_y and b_z. By definition, the pendulum lengths are related to the semi-axes by the expressions $\frac{1}{L_x}=\left.\frac{\partial^2 w}{\partial u^2}\right|_{\mathbf{0}}=\frac{b_z}{b_x^2}$ and $\frac{1}{L_y}=\left.\frac{\partial^2 w}{\partial v^2}\right|_{\mathbf{0}}=\frac{b_z}{b_y^2}$. These expressions show that there are ∞^1 possibilities of choosing b_x, b_y and b_z to obtain the desired L_x and L_y. Like in [10], the additional condition is here imposed by which b_z equals the geometric average of b_x and b_y, which ensures that the ellipsoid will degenerate into a sphere if $L_x = L_y$. With this position, L_x and L_y uniquely determine the ellipsoid as follows: $b_x = \sqrt[4]{L_x^3 L_y}$, $b_y = \sqrt[4]{L_x L_y^3}$ and $b_z = \sqrt{b_x b_y} = \sqrt{L_x L_y}$. Furthermore, $L_x \le L_y$ is assumed hereinafter for clarity, implying $b_x \le b_y$.

3.2.2 The friction pattern

As for the pendulum shape, also for the friction pattern the optimal solution obtained in Section 3.1 holds only locally around the origin. Eq. (4) is only one of the infinite possible ways to extend it elsewhere. If Eq. (4) is adopted together with Eq. (29), the friction pattern results:

$$\mu(\boldsymbol{q}) = \mu_0\|\nabla w\| = \mu_0\sqrt{\left(\frac{u^2}{L_x^2}+\frac{v^2}{L_y^2}\right)\Big/\left(1-\frac{u^2}{b_x^2}-\frac{v^2}{b_y^2}\right)} = \mu_0\,\|\boldsymbol{H}_w\boldsymbol{q}\|/[1-w(\boldsymbol{q})/b_z] \tag{30}$$

Based on Eq. (30):

(i) if $w(\boldsymbol{q}) \to 0$ then $\mu(\boldsymbol{q}) \approx \mu_0\|\boldsymbol{H}_w\boldsymbol{q}\| \to 0$ (around the origin);

(ii) if $w(\boldsymbol{q}) \to b_z$ then $\mu(\boldsymbol{q}) \to \infty$ (at the ellipsoid equator);

(iii) if $\mu(\boldsymbol{q}) = \bar{\mu}$ then $\left[\left(\frac{\mu_0}{\bar{\mu}}\right)^2\frac{1}{L_x^2}+\frac{1}{b_x^2}\right]u^2+\left[\left(\frac{\mu_0}{\bar{\mu}}\right)^2\frac{1}{L_y^2}+\frac{1}{b_y^2}\right]v^2 = 1$, which in the xy plane is the horizontal projection of the "iso-friction" line, locus of the ellipsoid having a constant friction coefficient $\bar{\mu}$. This projection is an ellipse whose aspect ratio, defined as the ratio of the major axis to the minor axis, is $\rho_{\bar{\mu}} = \sqrt{\left[\left(\frac{\mu_0}{\bar{\mu}}\right)^2\frac{1}{L_x^2}+\frac{1}{b_x^2}\right]\Big/\left[\left(\frac{\mu_0}{\bar{\mu}}\right)^2\frac{1}{L_y^2}+\frac{1}{b_y^2}\right]} \ge 1$.

Diving $\rho_{\bar{\mu}}$ by the aspect ratio $\rho_{\bar{w}} = b_y/b_x$ of any elliptic contour $w(\boldsymbol{q}) = \bar{w}$ of the ellipsoid, it results that $\rho_{\bar{\mu}}/\rho_{\bar{w}} = \sqrt{[(\mu_0/\bar{\mu})^2 b_y^2+1]/[(\mu_0/\bar{\mu})^2 b_x^2+1]}$ is a monotonic function of $\bar{\mu}$, decreasing from $b_y/b_x \ge 1$ (at the origin) to 1 (at the equator). In other words, projected on the horizontal plane the iso-friction lines are more slender ellipses than the contour lines. As a result: (a) the iso-friction lines are not plane curves and intersect the contour lines everywhere on the ellipsoid except along its principal meridians, where they are tangential to them; (b) along any iso-friction line w is maximum for $x = 0$ and minimum for $y = 0$, while along any contour line μ is maximum for $y = 0$ and minimum for $x = 0$. Obviously, if $L_x = L_y$ the ellipsoid turns into a sphere and the iso-friction lines coincide with the contour lines. For example, Figure 8 shows the friction pattern on an ellipsoid having $L_y = 2L_x$ (and then $b_x \cong 1.19L_x$, $b_y \cong 1.68L_x$ and $b_z = \sqrt{2}L_x$) and truncated at $w_{max} = b_z/2 = L_x/\sqrt{2}$. In the axonometric view, the z dimension is doubled for clarity's sake. A total of 11 contour lines are plotted (including the origin), uniformly spaced from 0 to w_{max}. Similarly, a total of 11 iso-friction lines are plotted (including the origin), uniformly spaced from 0 to $2\mu_0$.

3.2.3 Number and length of the viscous dampers

The optimal viscous damping coefficients c_x and c_y are obtained in Section 3.1 assuming only one damper in each horizontal direction. If more dampers are used in the same direction, the corresponding coefficient must be divided

among them. The length of the dampers is excluded from optimization and shall be chosen by the designer as deemed appropriate, considering that the longer the damper, the less sensitive its performance will be to second-order effects. In all following simulations, two dampers are assumed in each direction, symmetrically disposed around the z axis. Dampers 1 and 2 along x have coefficients $c_{x1} = c_{x2} = c_x/2$ and undeformed versors $\hat{\boldsymbol{c}}_{01} = -\hat{\boldsymbol{c}}_{02} = \hat{\boldsymbol{\imath}}$. Dampers 3 and 4 along y have coefficients $c_{y3} = c_{y4} = c_y/2$ and undeformed versors $\hat{\boldsymbol{c}}_{03} = -\hat{\boldsymbol{c}}_{04} = \hat{\boldsymbol{\jmath}}$. All dampers are given here the same length $l_{c0j} = \sqrt{L_x L_y} = b_z, j = 1{:}\,4$, for simplicity.

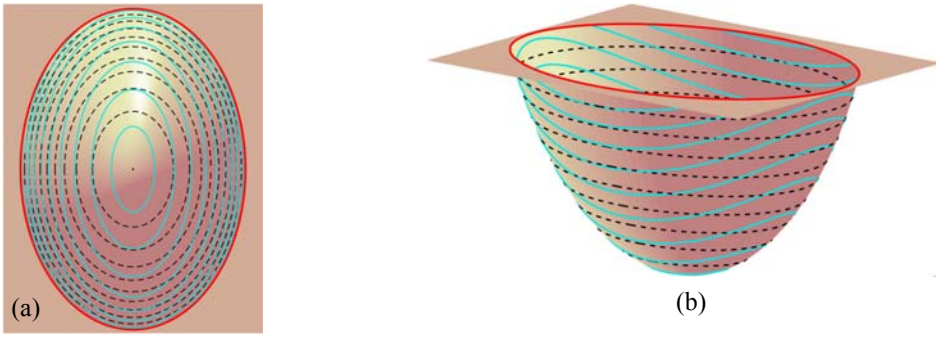

Figure 8. Intersection of contour lines (dashed black) and iso-friction lines (continuous azure) for $L_y/L_x = 2$: (a) xy view; (b) axonometric view (z dimension doubled for clarity's sake).

3.2.4 The bumper

The failsafe bumper is here excluded from optimization and modelled in a simplistic way, being of secondary interest in this study. Its constitutive components are the stiffness k_r, the damping coefficient c_r and the clearance w_r.
Stiffness and damping are here set to simulate a relatively rigid inelastic impact. Stiffness is set as $k_r = m\omega_r^2$, with $\omega_r = 20\sqrt{\omega_x \omega_y}$ [19]. Damping is set as $c_r = 2\zeta_r \omega_r m$, with $\zeta_r = -\frac{\ln e_r}{\sqrt{\pi^2 + \ln^2 e_r}}$, e_r being the elastic restitution coefficient [20]. With $e_r = 0.5$, here $\zeta_r = 0.2155$. Finally, unless otherwise specified, clearance is set as $w_r = b_z/2$, meaning that the bumper is engaged when the absorber reaches half the height of the ellipsoid equator.

4. Simulations in the small-displacement domain

In this section, the optimal V-BTMD and HT-BTMD are compared in the small-displacement domain. First 2D models and then 3D models are considered, under white-noise ground motions or real seismic records. The structural damping ratio is set at 2% in all simulations.

4.1 2D models

The simplified first-order 2D model expressed by Eq. (26) is adopted. Despite their bidirectionality, BTMDs are here used only along one direction. Two types of input are considered: (i) white-noise accelerations; (ii) real seismic records. In this latter case, the BTMD robustness to variations of the viscous and friction damping ratios is discussed.

4.1.1 White-noise ground accelerations

With the BTMDs optimized in H_∞ terms (Table 1), Eq. (26) is adopted with $\ddot{u}_g$ assigned as a stationary Gaussian zero-mean white-noise process. For both the uncontrolled structure and the structure controlled by the V-BTMD, the system is time-invariant and linear; its stationary root-mean-square (rms) response can be obtained from the state and output covariance matrices, on their turn computed by solving the Lyapunov equation [17]. For the structure controlled by the HT-BTMD, instead, the system is time-invariant and homogeneous but nonlinear; its stationary rms response must be computed through Monte Carlo simulations, by averaging the system rms response to many realizations of the stochastic input process.
For example, 100 realizations are here considered, each one having a duration of $3600T_{sx}$ and a sampling time of $0.01T_{sx}$, where $T_{sx} = 2\pi/\omega_{sx}$ is the structural period. By denoting as $\mathrm{rms}(u_s)$, $\mathrm{rms}(u)$ and $\mathrm{rms}(\dot{u}_s)$ the rms of, respectively, the structural displacement, the TMD stroke and the structural velocity, the control performance is expressed by the following three response ratios, defined by normalizing the controlled to the uncontrolled rms responses: $R_d = \mathrm{rms}(u_s)_{con}/\mathrm{rms}(u_s)_{unc}$, $R_s = \mathrm{rms}(u)_{con}/\mathrm{rms}(u_s)_{unc}$ and $R_v = \mathrm{rms}(\dot{u}_s)_{con}/\mathrm{rms}(\dot{u}_s)_{unc}$. For the two BTMD types, R_d, R_s and R_v are reported in Figure 9 for different values of m_{Rx} ranging from 1‰ to 20%. The V-BTMD and the HT-BTMD result to be substantially equivalent against white-noise accelerations.

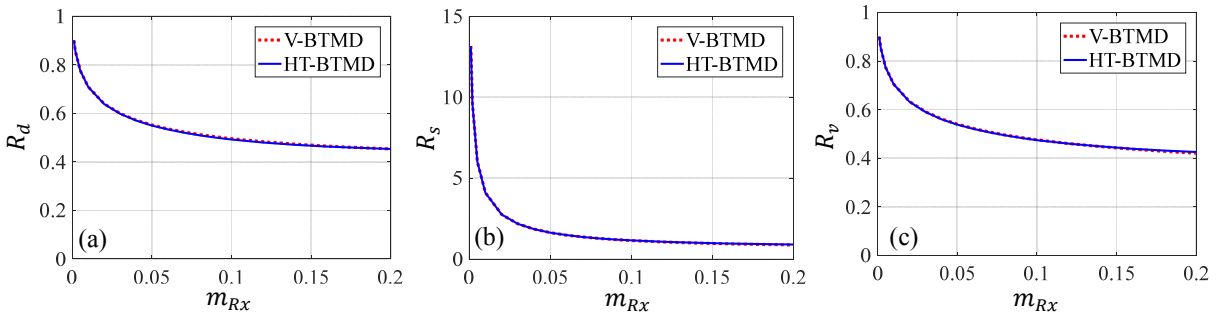

Figure 9. First-order 2D model under white-noise ground accelerations. Rms response ratios as a function of m_{Rx}, in terms of: (a) structural displacement; (b) BTMD stroke; and (c) structural velocity.

4.1.2 Real seismic ground motions – Nominal performance

With the BTMDs optimized in H∞ terms (Table 1), Eq. (26) is adopted with $\ddot{u}_g$ assigned as a real seismic record. Simulations are repeated by subjecting the structure, uncontrolled or controlled, to an entire set of records, and by varying, for each record, the structural period T_{sx} in the range 0.1÷6.0 s, in order to draw uncontrolled and controlled response spectra. The set is the one already used in [21], which includes 338 horizontal components of near-field records extracted from the PEER NGA Strong Motion Database. Correspondingly, 338 spectra are computed for each system configuration (uncontrolled, V-BTMD-controlled, HT-BTMD-controlled) and for the three response quantities herein chosen to describe the control performance, including: (i) the maximum structural displacement $u_{s,max}$; (ii) the maximum BTMD stroke u_{max}; (iii) the rms structural velocity $\dot{u}_{s,rms}$. For each configuration and for each response, the 338 spectra are first condensed into their respective rms spectrum, and then the following rms response ratio spectra are derived by dividing the controlled by the uncontrolled rms response spectra [21]:

- $R_{dx} = \text{rms}(u_{s,max})_{con}/\text{rms}(u_{s,max})_{unc}$ (structural displacement)
- $R_{sx} = \text{rms}(u_{max})_{con}/\text{rms}(u_{s,max})_{unc}$ (BTMD stroke)
- $R_{vx} = \text{rms}(\dot{u}_{s,rms})_{con}/\text{rms}(\dot{u}_{s,rms})_{unc}$ (structural velocity)

Results are shown in Figure 10 for the two BTMD types and for the three mass ratios m_{Rx} = 1%, 3% and 10%. As for the white-noise ground acceleration, the V-BTMD and the HT-BTMD still exhibit a nearly identical performance.

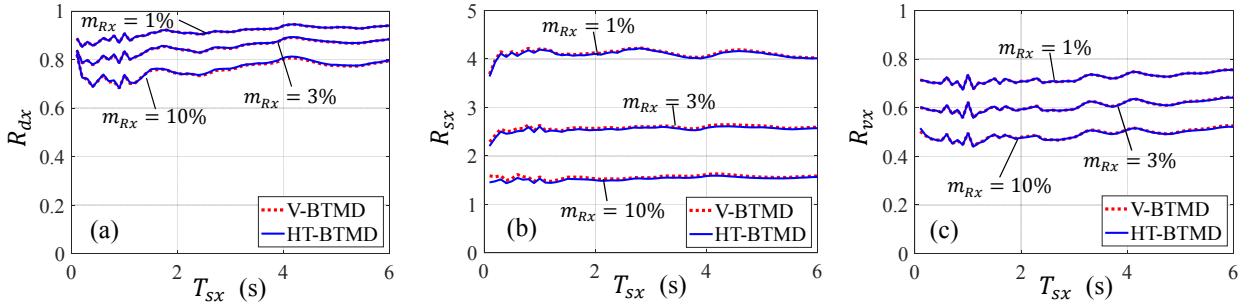

Figure 10. First-order 2D model under the chosen set of records. Rms response ratio spectra for m_{Rx} = 1%, 3%, 10%, in terms of: (a) structural displacement; (b) BTMD stroke; (c) structural velocity; and (d) structural acceleration.

4.1.3 Real seismic ground motions – Robust performance

If the viscous damping ratio ζ_x of the V-BTMD and the friction damping ratio μ_{0x} of the HT-BTMD are different from their H∞ optimal values ζ_{xopt} and μ_{0xopt}, and in fact equal to the latter times an uncertainty factor δ, the rms response ratio spectra change as exemplified in Figure 11, where the cases δ = 0.5 and 2 are compared with the nominal case δ =1. For brevity, results are reported only for m_{Rx} = 3%, the cases for m_{Rx} = 1% and m_{Rx} = 10% showing similar trends. As expected, the BTMD stroke R_{sx} is strongly (and inversely) influenced by damping variations. On the other hand, R_{dx} and R_{vx} are worsened for $\delta = 2$ but scarcely modified for $\delta = 0.5$. In fact, $\delta = 0.5$ implies minor increments of R_{vx} and unexpected small reductions of R_{dx}, suggesting that the adopted H∞ optimal damping is larger than optimal for controlling the selected set of records. Interestingly, the V-BTMD and the HT-BTMD continue to show a similar performance even under damping variations, which proves that the HT-BTMD is not less robust than an ordinary V-BTMD.

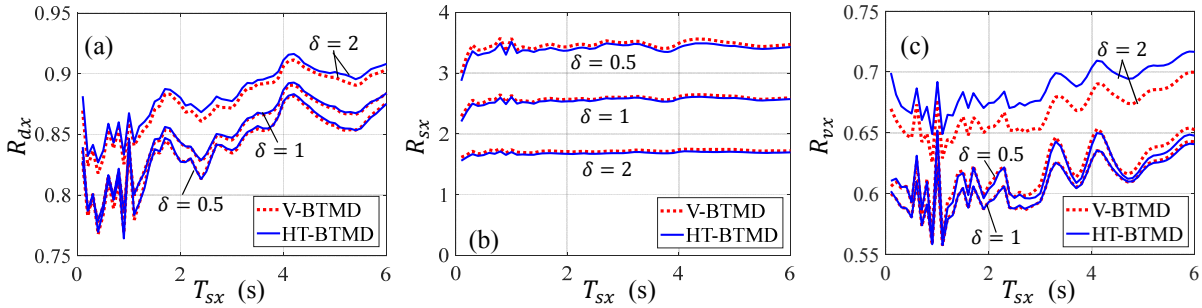

Figure 11. First-order 2D model under the set of records. Rms response ratio spectra for m_{Rx} = 3% and for δ = 0.5, 1 and 2.

4.2 3D models

The bidirectional performance of the V-BTMD and the HT-BTMD under the same set of real seismic records is here verified by adopting the first-order 3D model expressed by Eq. (22). As explained in Section 3, optimization is conducted separately in the two horizontal directions, resulting in identical dimensionless BTMD parameters along x and y because of the assumed identity of structural damping and modal masses in both directions. Based on this model, the equations of motion along x and y are still linear and uncoupled for the V-BTMD but nonlinear and coupled by the friction term for the HT-BTMD. To investigate how, because of friction coupling, the HT-BTMD performance is influenced by the ratio T_{sy}/T_{sx} between the two structural target periods, rms response ratios spectra are here computed by: (i) first, fixing T_{sy}/T_{sx} = 1 and varying $T_{sx} = T_{sy}$ in the range 0.5:0.5:4 s (Figure 12); and (ii) then, fixing T_{sx} = 2 s and varying T_{sy}/T_{sx} in the range 1:0.1:2 (Figure 13). The mass ratio m_R (the subscript x being here removed because $m_{Rx} = m_{Ry} = m_R$) is alternatively taken as 1%, 3% or 10%. Spectra are reported in terms of the following 3D rms response ratios, obtained by averaging the corresponding 2D rms response ratios along x and y: (i) $R_d = \sqrt{R_{dx}R_{dy}}$ (structural displacement); (ii) $R_s = \sqrt{R_{sx}R_{sy}}$ (BTMD stroke); (iii) $R_v = \sqrt{R_{vx}R_{vy}}$ (structural velocity).

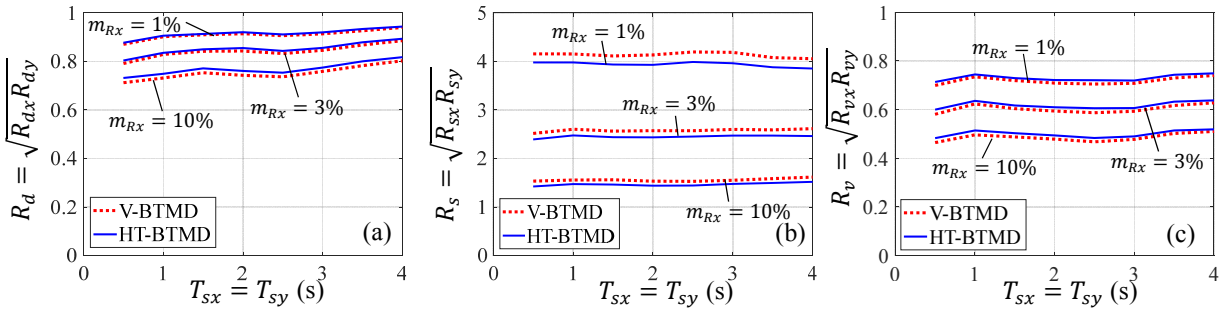

Figure 12. First-order 3D model under the set of records. 3D rms response ratio spectra for $T_{sx} = T_{sy}$ and m_{Rx} = 1%, 3%, 10%.

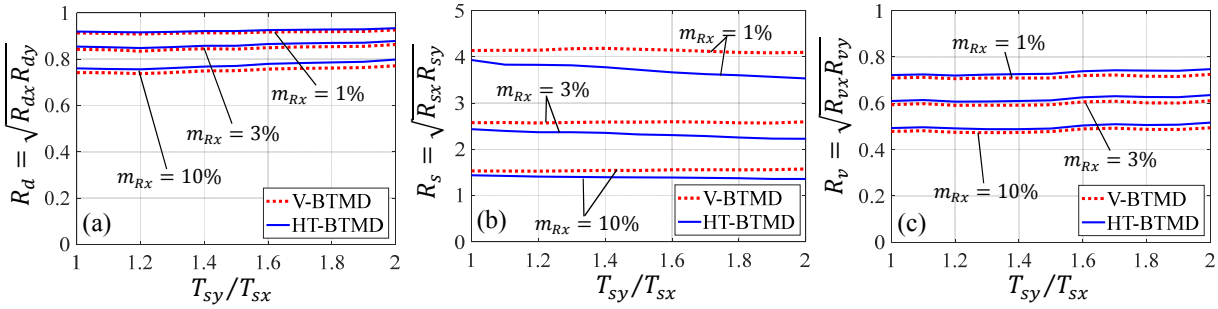

Figure 13. First-order 3D model under the set of records. 3D rms response ratios as a function of T_{sy}/T_{sx} for T_{sx} = 2 s and for m_{Rx} = 1%, 3% and 10%.

Figure 12 shows that under bidirectional shaking, because of friction coupling, the HT-BTMD spectra no longer nearly coincide with the V-BTMD spectra (Figure 10), but are systematically higher for R_d and R_v and lower for R_s. If a smaller BTMD stroke is generally welcome, a larger structural response certainly is not, so friction coupling proves detrimental for the HT-BTMD and responsible for a 3D performance reduction. The extent of this reduction is however quite limited, as visible in Figure 12. Moreover, improvements of the friction pattern are already under study, which might completely solve the problem. Figure 13 shows that these trends are scarcely affected by the ratio T_{sy}/T_{sx}.

5. Simulations in the large-displacement domain

In this section, the optimal V-BTMD and HT-BTMD are compared in the large-displacement domain based on the fully nonlinear model described by Eq. (14), in order to show the dependence of the BTMD performance on the excitation intensity. First 2D models and then 3D models are considered, still using a 2%-damped SDOF representation of the primary structure in each direction.

5.1 2D models

The same problem described in Section 4.1.2 is here treated in the large-displacement domain, under increasing seismic intensities. For T_{sx} equal to either 0.5 s or 4 s, Figure 14 shows R_{dx}, R_{sx} and R_{vx} as a function of the input intensity ratio I ranging from 0^+ to 1, I being the dimensionless factor used to scale the entire set of records. Together with the V-BTMD and the HT-BTMD, a third option is here included, denoted as HT-BTMD*, representing an HT-BTMD having friction pattern $\mu(\boldsymbol{q}) = \mu_0\|\boldsymbol{H}_w\boldsymbol{q}\|$ instead of $\mu(\boldsymbol{q}) = \mu_0\|\nabla w\|$, for any value of $\boldsymbol{q}$. The HT-BTMD* coincides with the HT-BTMD in the small-displacement domain, in this case ensuring the same homogeneous law, but in the large-displacement domain provides a less steep, distance-proportional friction pattern.

For $I = 0^+$, Figure 14 confirms the first-order results already obtained in Section 4.1.2. As I increases, the effectiveness worsens (R_{dx} and R_{vx} increase) and the BTMD stroke decreases because of bumping, for both structural periods and for all BTMD types. However, variations are large only for T_{sx} = 0.5 s because of the limited stroke capacity typical of small-period pendulum BTMDs [10], and appear in this case dependent on the BTMD type, with the V-BTMD showing the worst performance and the HT-BTMD the best one. This superiority of the HT-BTMD can be attributed to the progressively increasing damping provided, with respect to I, by its friction pattern, compared to the progressively decreasing damping ensured by the viscous dampers under large displacements. The HT-BTMD* sets somewhere in between, proving an interesting alternative to the gradient-proportional friction pattern, characterized by a less rapid friction increase and ultimately by a reduced maximum friction coefficient along the surface.

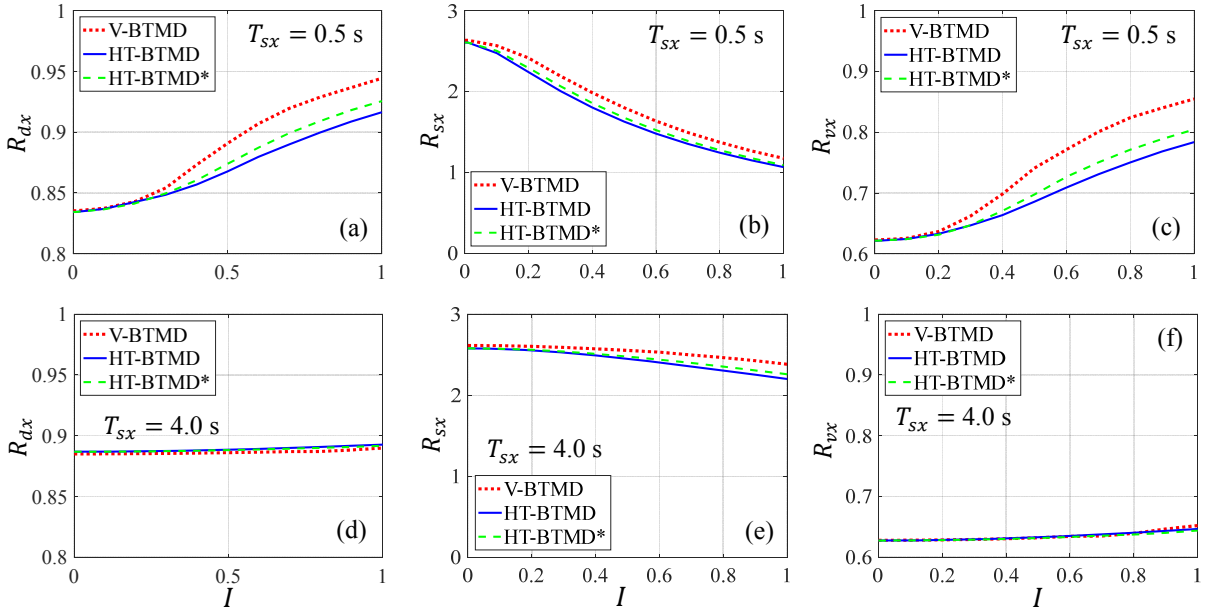

Figure 14. Second-order 2D model under the chosen set of records. Rms response ratios as a function of the input intensity ratio I for T_{sx} = 0.5 s (figures a to c) or T_{sx} = 4.0 s (figures d to f), and for m_{Rx} = 3%.

5.2 3D models

The same problem described in Section 4.2 is here treated in the large-displacement range, under increasing seismic intensities. Results are reported in Table 2 for m_R = 3%, by comparing three input intensity ratios, I = 0, 0.5 or 1, and four combinations of structural periods, with T_{sx} = 1 s or 4 s and T_{sy}/T_{sx} = 1 or 1.5. An additional rms response ratio is there reported as well, R_a, referred to the absolute acceleration of the primary structure. Table 2 confirms that under bidirectional motion the most effective option is the V-BTMD as long as second-order effects are negligible (i.e. for T_{sx} = 4 s or I = 0), and the HT-BTMD in all other cases. While looking at the performance degradation associated to large intensities and small periods (see again Figure 14), it should be recalled that the adopted set of records represents extreme near-field earthquakes, so the presented scenario can be regarded as prudential.

Table 2. Second-order 3D model under the selected set of records, for m_R = 3%. Rms response ratios for different structural periods and intensity ratios.

R_i	Type	$T_{sx} = T_{sy}$ = 1 s			T_{sx} = 1 s T_{sy} = 1.5 s			$T_{sx} = T_{sy}$ = 4 s			T_{sx} = 4 s T_{sy} = 6 s		
		I= 0	I= .5	I= 1	I= 0	I= .5	I= 1	I= 0	I= .5	I= 1	I= 0	I= .5	I= 1
R_d	V-BTMD	0.83	0.90	0.95	0.84	0.88	0.94	0.89	0.89	0.89	0.88	0.89	0.89
	HT-BTMD	0.84	0.88	0.92	0.85	0.87	0.91	0.89	0.89	0.90	0.90	0.90	0.90
R_s	V-BTMD	2.60	1.81	1.16	2.58	2.00	1.38	2.61	2.57	2.45	2.60	2.60	2.49
	HT-BTMD	2.47	1.52	1.00	2.35	1.64	1.15	2.46	2.32	2.05	2.30	2.22	2.04
R_v	V-BTMD	0.62	0.78	0.89	0.61	0.73	0.85	0.63	0.63	0.65	0.64	0.64	0.66
	HT-BTMD	0.64	0.71	0.80	0.63	0.68	0.76	0.64	0.64	0.66	0.65	0.66	0.67
R_a	V-BTMD	0.82	0.87	0.92	0.82	0.86	0.91	0.87	0.87	0.87	0.87	0.88	0.88
	HT-BTMD	0.83	0.85	0.88	0.84	0.86	0.88	0.88	0.88	0.89	0.89	0.89	0.89

6. Case study

In this section, an H_∞ optimal BTMD of either viscous or friction type is simulated on an MDOF structural model representative of existing medium-rise standard office buildings in high seismic hazard regions. The model is a slight variant of the 9-storey steel MRF building model proposed for the Los Angeles (LA) area within the SAC Phase II Steel Project [22], and later turned into one of the three benchmark control problems for seismically excited nonlinear buildings [23]. Compared to the original model, having in-plane symmetry and fundamental periods $T_{sx} = T_{sy}$ = 2.26 s, the variant herein adopted scales the stiffness matrix along x and y so that T_{sx} = 2 s and T_{sy} = 2.4 s, to generalize the design scenario. A 2% structural damping is assumed in every mode. The BTMD mass is set at 5% the total building mass. According to Warburton's classical approach [2], the corresponding 'effective' mass ratio (as "seen" by the target mode) results m_R = 11.3% in both horizontal directions. Entering in Table 1 with m_R = 11.3% and interpolating between the lines provides the optimal dimensionless parameters for, respectively, the V-BTMD and the HT-BTMD. Table 3 reports such parameters in columns 2 to 4, and the corresponding dimensional parameters in the subsequent columns. It can be observed that: (i) the friction ratio μ_0 is 0.574, sufficiently far from unity to ensure the HT-BTMD re-centring capability even under large uncertainties; and (ii) the ellipsoidal pendulum (having semi-axes b_x, b_y and b_z) is smaller for the HT-BTMD because of its greater frequency ratio ω_R. To limit the pendulum dimensions, the bumper clearance ω_r is equalled to only b_z/4 in this case. Figure 15a shows a lateral view of the building-BTMD model. The BTMD is conceived as an additional floor resting on 16 identical single-concave sliding pendulum bearings (Figure 1d), coaxial with the building inner columns. The floor projects over the outer bearings to ensure the same compression in each bearing. Figure 15b schematizes the HT-BTMD bearing. Display of the bumper is omitted for brevity. Might the single-concave bearing be considered impractically large, the same equivalent pendulum could be realized by using two cavities facing each other (Figure 1e), resulting in half the size of the single cavity [10].

Table 3. Design parameters for the BTMDs on the 9-storey benchmark building.

	ω_R (-)	ζ (-)	μ_0 (-)	T_x (s)	T_y (s)	L_x (m)	L_y (m)	b_x (m)	b_y (m)	b_z (m)	l_{c0j} (m)	ω_r (m)
V-BTMD	0.859	0.204	-	2.33	2.79	1.35	1.94	1.48	1.77	1.62	1.62	0.40
HT-BTMD	0.939	-	0.574	2.13	2.55	1.13	1.62	1.23	1.48	1.35	-	0.34

Table 4 compares the performance of the two absorbers, evaluated by subjecting the 9-storey building to five sets of records of increasing intensity (with return periods correspondently varying from 7.2 to 2475 years). Each set, defined in accordance with LA seismic hazard, consists of ten 2-component records, alternatively applied to the structure with incident angles of 0° and 90°. Further details on records selection are available in [24]. Performance is expressed in Table 4 by the four 3D rms response ratios R_d to R_a and by two further quantities: (i) % bumps, defined as the percentage of records in which the bumper gets activated; (ii) $R_\mu = \mathrm{rms}(\max(\mu))$, defined as the rms of the maximum value of the friction coefficient met during motion.

Table 4 shows that, as long as bumping is avoided or limited, which happens under the first four sets of records (i.e. for return periods ≤ 475 years), the two types show nearly the same good performance, with the V-BTMD slightly more effective in terms of response reduction and the HT-BTMD slightly better in terms of strokes. However, if second order effects and bumping further increase, which happens under the fifth set (i.e. for a return period of 2475 years), the performance significantly reduces for both BTMDs, especially in terms of accelerations for the HT-BTMD type. Anyway, because most lifecycle cost advantages of a TMD are in fact related to medium-intensity frequent earthquakes rather than to extreme events, as recently shown in [24] for the same building and the same seismic hazard herein considered, the overall control performance portrayed by Table 4 is still satisfactory. In all cases, R_μ never exceeds 0.61, a value still compatible with sliding between ordinary structural materials.

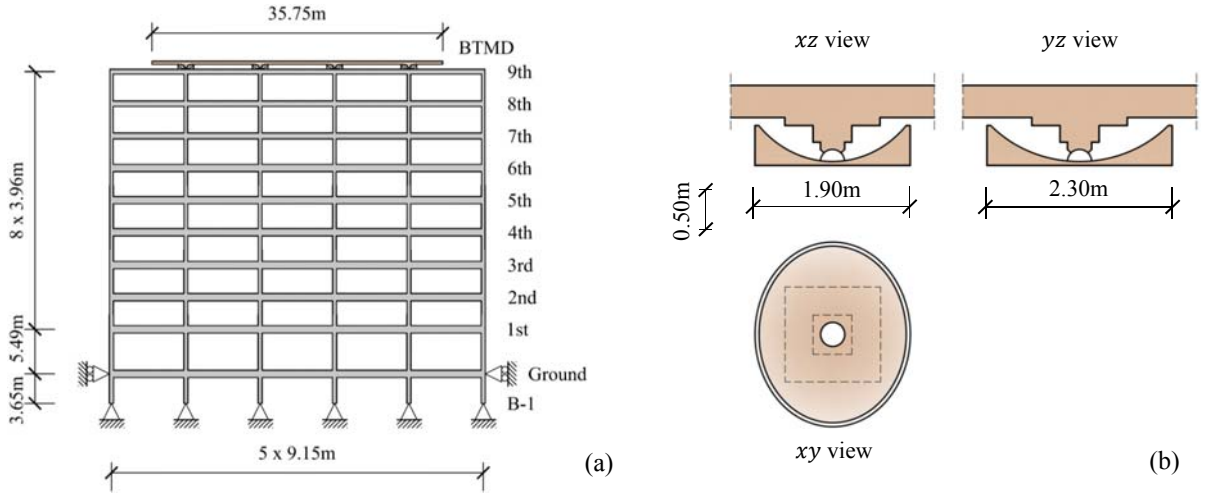

Figure 15. Case study: (a) lateral (xz) view of the building model with the BTMD; (b) schematics of the pendulum bearing for the HT-BTMD system (bumper omitted for brevity).

Table 4. Performance of the BTMDs on the 9-storey benchmark building under increasing seismic intensities.

Performance	Type	Return period for each set of records (years)				
		7.2	14.4	72	475	2475
R_d	V-BTMD	0.74	0.74	0.74	0.79	0.92
	HT-BTMD	0.76	0.76	0.76	0.80	0.91
R_s	V-BTMD	1.32	1.31	1.30	1.22	0.70
	HT-BTMD	1.27	1.27	1.21	1.01	0.59
R_v	V-BTMD	0.65	0.65	0.65	0.63	0.81
	HT-BTMD	0.66	0.66	0.67	0.64	0.82
R_a	V-BTMD	0.92	0.92	0.92	1.03	1.10
	HT-BTMD	0.93	0.93	0.93	1.27	1.76
% bumps	V-BTMD	0	0	0	55	100
	HT-BTMD	0	0	0	65	100
rms(max(μ))	HT-BTMD	0.03	0.06	0.22	0.51	0.61

7. Experimental testing

To prove the validity and feasibility of the HT-BTMD concept, a small-scale prototype of absorber is built and tested.

7.1 Prototype description

The device, conceived as a double-cavity rolling-pendulum BTMD (Figures 1c and 2a), consists of two aluminum plates, having dimensions 400x300x25 mm^3 and hosting three cavities each (Figure 16a). The three pairs of corresponding cavities sandwich three polypropylene balls having 30 mm diameter. The cavities are in the shape of a torus, except for their inner region, raised with respect to the torus by an offset of 0.18 mm (Figure 16b). Around this inner region, which is left uncoated, each cavity presents two successive elliptic annular regions, coated with two different types of commercial adhesive tapes, both 0.18 mm thick (Figures 16a and 17a). The internal annular region is covered with a PVC-coated ordinary tape (black), while the external one is covered with a PE-coated duct tape reinforced with a PE cloth (silver). Thus, each cavity presents, after coating, a toroidal rolling surface (having principal curvature radii R_x = 29.87 mm and R_y = 54.71 mm), divided in three regions, each characterized by a different surface material: (1) aluminum (inner region); (2) normal tape (intermediate region); (3) cloth tape (outer region). The three regions have different dimensions depending if they belong to the lower or to the upper plate (Figure 17a). This ensures that, during rolling, the contact between each ball and both plates can happen according to five possible combinations of surface materials, depending on the position of the ball relative to the lower plate (which is also equal to the position of the upper plate relative to the ball, because of the no-slipping condition). As shown in Figure 17b, these five combinations correspond to five possible domains for the position of the contact point C relative to the lower cavity, in fact obtained by intersecting the horizontal projections of the lower and the upper regions. Because materials 1 to 3 exhibit a progressively increasing rolling friction coefficient, the five domains ensure the device a 5-level stepwise increasing friction, potentially capable to discretely approximate the desired homogeneous friction pattern. In practice, the accuracy of the approximation requires an appropriate choice of surface materials and domains dimensions. In the

present case, the surface materials are selected through preliminary free-vibration tests conducted on auxiliary plates (the same already used in [10]), whose simple toroidal cavities (having no raised inner region) are in turn uniformly coated with a single adhesive layer. The friction coefficient is thus identified for several combinations of coating materials and thicknesses, and the convenient sequence of contact surfaces is finally selected which ensures a gradual increase of μ. The domains dimensions are consequently established by approximately fitting, along both x and y, the linearly increasing desired friction pattern through the stepwise increasing available friction coefficients.

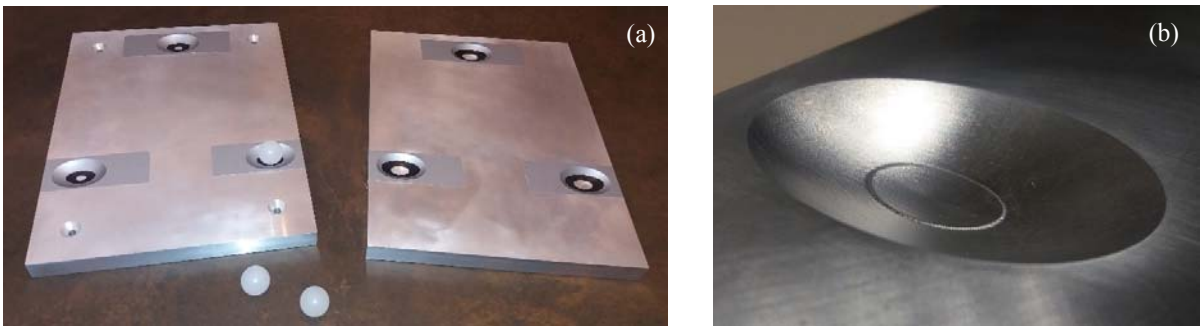

Figure 16. HT-BTMD prototype: (a) the device components (lower plate on the left, upper plate on the right, and three rolling balls); (b) one of the upper plate cavities before coating (clearly visible its raised inner region).

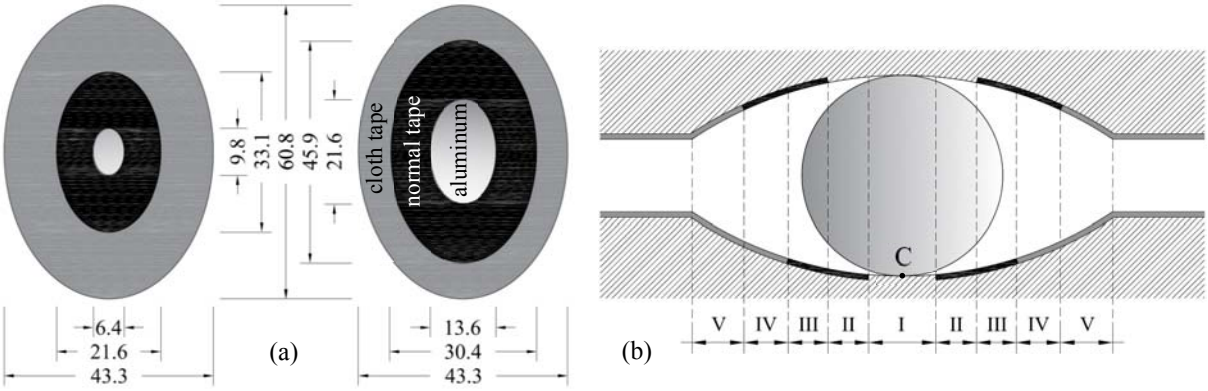

Figure 17. HT-BTMD prototype: (a) dimensions of the three regions of each cavity (planar views); (b) identification of the five contact domains (sectional view, the coating thickness not in scale).

7.2 Testing program

The HT-BTMD prototype is then tested in both free- and forced-vibration conditions. Free-vibration tests are performed by imparting an initial relative displacement to the upper plate while keeping fixed the lower plate. Forced-vibration tests are performed by imparting the lower plate a Gaussian white noise acceleration through a unidirectional shake table. In both types of tests accelerometers are installed on the upper plate to measure its response along x and y; in forced-vibration tests an accelerometer is additionally installed on the lower plate in the direction of motion.

7.3 Experimental results

Figures 18a and 18b report some results from free-vibration tests, respectively along x and y. The experimental accelerations of the upper plate (red curves) are compared with the simulated accelerations (blue curves), based on the fully nonlinear model given by Eqs. (1) to (3) and (7) to (11), with the two friction ratios in Eq. (3) taken as μ_{0x} = 4.34% and μ_{0y} = 4.91%. A very close matching appears between the experimental and the simulated responses, indicating that the realized stepwise friction mechanism can properly reproduce the homogeneous friction concept.

Figures 19a and 19b show some results from forced-vibration tests, along x and y. The experimental and simulated linearized transfer functions, computed from the lower plate acceleration to the upper plate acceleration, are reported for three excitation levels (characterized through the rms value of the acceleration input). They match quite well and show a small sensitivity to the excitation level, proving the amplitude-independence of the HT-BTMD performance.

For comparison, Figures 20a and 20b show the free- and forced-vibration experimental response (along both x and y) of the above-mentioned auxiliary plates, when their cavities are uniformly coated with the black PVC normal tape.

The free-response curves in Figure 20a show the linearly decreasing trend typical of constant friction (instead of the nearly exponential decreasing trend typical of homogeneous friction, apparent in Figure 18). Accordingly, the transfer functions in Figure 20b show significant variations with the input amplitude, implying a much lesser robustness of the control performance with respect to the HT-BTMD device.

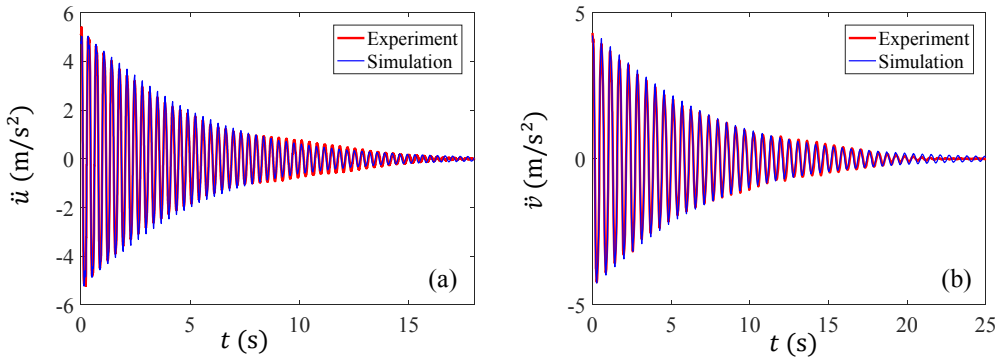

Figure 18. Free-vibration tests of the HT-BTMD prototype. Experimental and simulated accelerations along: (a) x; (b) y.

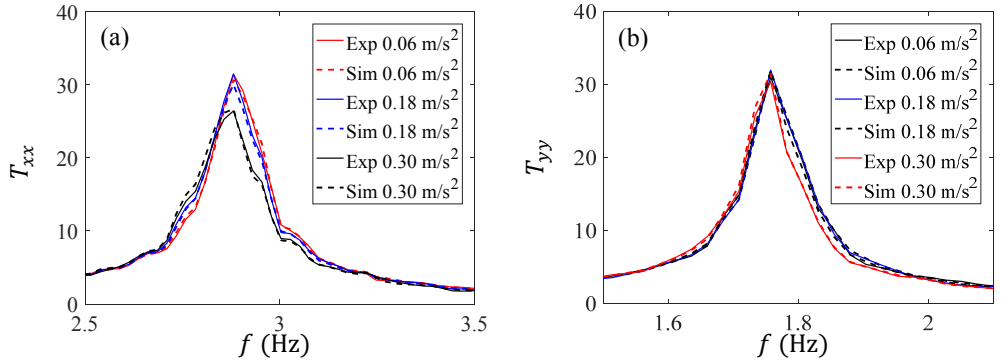

Figure 19. Forced-vibration tests of the HT-BTMD prototype. Experimental and simulated acceleration transfer functions for different rms values of the acceleration input, respectively along: (a) x; (b) y.

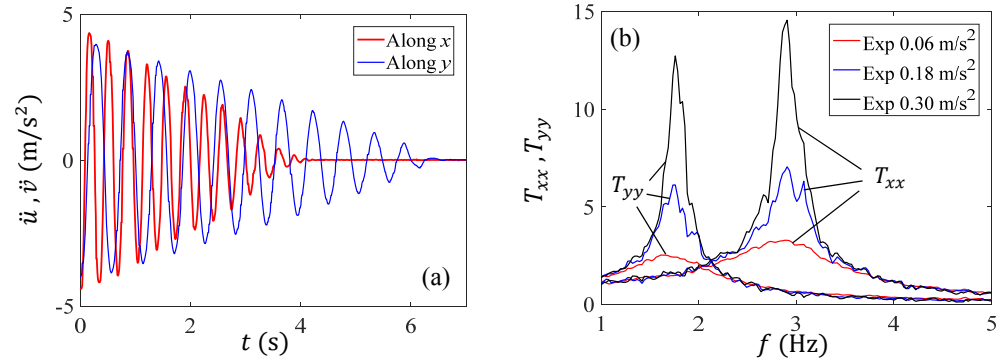

Figure 20. (a) Free- and (b) forced-vibration experimental response of the auxiliary plates when their cavities are uniformly coated with the black PVC tape. Results along *x* and *y* superimposed in both figures, for brevity.

8. Conclusion

This paper proposes a novel concept of bidirectional pendulum TMD, called the HT-BTMD, in which dissipation is provided by rolling or sliding friction, with the friction coefficient spatially varying along the pendulum surface proportionally to the modulus of the surface gradient. Such a friction pattern ensures: (i) a nonlinear but homogeneous bidirectional dissipation model in the small-displacement domain, which makes the HT-BTMD performance independent from the excitation intensity, and (ii) an appropriate increase of the equivalent damping with the absorber stroke in the large-displacement domain, which delays control degradation. With respect to existing bidirectional pendulum TMDs, the HT-BTMD does not need to incorporate specific viscous or friction dashpots, thus ensuring a greater compactness (often desirable in TMD applications) and possibly a reduced cost.

After deriving the HT-BTMD fully nonlinear model, the paper proposes a method for its H_∞ optimal design, which provides, as a function of the assigned mass ratio, the two tuning parameters of the absorber (i.e. frequency ratio and friction ratio) ensuring the minimal worst-case structural response to an harmonic input.
By extensive numerical simulations of the new HT-BTMD and of its ordinary viscous analogue, the V-BTMD, the following main conclusions are drawn:
1) The HT-BTMD proves substantially equivalent to the V-BTMD in most cases, and particularly when involved in unidirectional motion occurring in the small displacement domain. Minor differences include: (i) a slight superiority of the V-BTMD under bidirectional motion in the small displacement domain; and (ii) a slight superiority of the HT-BTMD in the large-displacement domain.
2) Both types undergo performance degradation if the stroke demand is larger than their stroke capacity, which typically occurs for rigid structures subjected to large excitations. This drawback has already been reported for the V-BTMD and is confirmed for the HT-BTMD, although partially attenuated by its greater dissipation capability at large displacements. Despite such degradation, in all examined cases both devices still ensure a significant degree of mitigation, so that their overall performance still appears satisfactory in a lifecycle cost perspective.
The validity and feasibility of the concept are demonstrated through experimental tests of a small-scale HT-BTMD prototype, which also show the efficacy of a stepwise discretization of the optimal homogeneous friction pattern.
In conclusion, the new device proves a viable alternative to viscously damped pendulum TMDs. It can be realized as a 3D or as a 2D device, using a continuously or discretely varying friction pattern. The proposed H_∞ optimization method can be applied to any other class of homogeneous friction TMD. The novel concept of a homogeneous tangential friction can be extended to other application fields, including base isolation.

References

1. Soong TT, Constantinou MC. Passive and Active Structural Vibration Control in Civil Engineering, Springer Verlag, New York, USA, 1994.
2. Warburton GB. Optimum absorber parameters for various combinations of response and excitation parameters. Earth Eng Struct Dyn 1982;10:381-401.
3. Náprstek J, Fischer C, Pirner M, Fischer O. Non-linear model of a ball vibration absorber. Comput Meth Applied Sciences 2013;30:381-396.
4. Legeza VP. Dynamics of vibroprotective systems with roller dampers of low-frequency vibrations. Strength Mat 2004;36/2:185-194.
5. Matta E, De Stefano A. Robust design of mass-uncertain rolling pendulum TMDs for the seismic protection of buildings. Mech Syst Sign Proc 2009;23:127-147.
6. Bransch M. Unbalanced oil filled sphere as rolling pendulum on a flat surface to damp horizontal structural vibrations. J. Sound Vibr 2016;368:22-35.
7. Chen J, Georgakis CT. Tuned rolling-ball dampers for vibration control in wind turbines. J Sound Vibr 2013;332:5271-5282.
8. Wang J, Wierschem NE, Spencer BF Jr, Lu X. Track nonlinear energy sink for rapid response reduction in building structures. J Eng Mech 2015;141/1:1-10.
9. Wang J, Wierschem NE, Spencer BF Jr, Lu X. Numerical and experimental study of the performance of a single-sided vibro-impact track nonlinear energy sink. Earthq Eng Struct Dyn 2016;45:635-652.
10. Matta E, De Stefano A, Spencer BF Jr. A new passive rolling-pendulum vibration absorber using a non-axial-symmetrical guide to achieve bidirectional tuning. Earthq Eng Struct Dyn 2009;38:1729-1750.
11. Almazan JL, De la Llera JC, Inaudi JA, Lopez-Garcia D, Izquierdo LE. A Bidirectional and homogeneous tuned mass damper: a new device for passive control of vibrations. Eng Struct 2007;29:1548-1560.
12. Inaudi J, Kelly J. Mass damper using friction-dissipating devices. J Eng Mech 1995;121:142-149.
13. Ricciardelli F, Vickery BJ. Tuned vibration absorbers with dry friction damping. Earthq Eng Struct Dyn 1999;28/7:707-723.
14. Chung LL, Wu LY, Lien KH, Chen HH, Huang HH. Optimal design of friction pendulum tuned mass damper with varying friction coefficient. Struct Control Health Monit 2013;20: 544-559.
15. Zhang Z-L, Chen J-B, Li J. Theoretical study and experimental verification of vibration control of offshore wind turbines by a ball vibration absorber. Struct Infrastr Eng 2014;10/8:1087-1100.
16. Li S, Fu L, Kong F. Seismic response reduction of structures equipped with a voided biaxial slab-based tuned rolling mass damper. Shock and Vibration 2015; 760394:1-15.
17. Burl JB. Linear Optimal Control. Addison-Wesley, Longman, Reading, MA, Menlo Park, CA, USA, 1999.
18. Leung AYT, Zhang H. Particle swarm optimization of tuned mass dampers. Eng Struct 2009;31: 715-728.
19. Lu Z, Wang Z, Masri SF, Lu X. Particle impact dampers: past, present, and future. Struct Control Health Monit 2017;e2058: 1-25.
20. Shäfer J, Dippel S, Wolf D. Force schemes in simulations of granular materials. Journal de Physique I, EDP Sciences 1996;6/1:5-20.
21. Matta E. Performance of tuned mass dampers against near-field earthquakes. Struct Eng Mech 2011;39/5:621-642.
22. Gupta A, Krawinkler H. Seismic demands for performance evaluation of steel moment resisting frame structures. The John A. Blume Earthquake Engineering Center, Stanford University, Stanford, CA, Report No. 132, 1999.
23. Ohtori Y, Christenson RE, Spencer BF Jr, Dyke SJ. Benchmark control problems for seismically excited nonlinear buildings. J Eng Mech 2004;130/4:366-385.
24. Matta E. Lifecycle cost optimization of tuned mass dampers for the seismic improvement of inelastic structures. Earthq Eng Struct Dyn 2017;1-24, https://doi.org/10.1002/eqe.2987.